Search for Superpartner of Electron and Muon in the e^+e^- Reactions up to the $\sqrt{s}$ of 61.4 GeV

Atsushi Taketani

Department of Physics, Hiroshima University

Higashi-senda-machi, Naka-ku, Hiroshima, 730, Japan

January 1990

Abstract

An experimental search for scalar electron and scalar muon, the supersymmetric partner of electron and muon, has been performed at TRISTAN e^+e^- collider at the National Laboratory of High Energy Physics, using the VENUS detector. The study has been made at center-of-mass energies from 55 to 61.4GeV with an integrated luminosity of 29.2pb^{-1}. No events which are due to scalar electron or scalar muon are observed and lower mass limits are obtained as functions of photino mass.

Contents

Chapter 1

Introduction

The current theoretical picture of physics, which is often referred to as the standard model [1], successfully describes interactions between elementary particles in the wide energy range from 10^6 eV to 10^{11} eV. The standard model is, however, not a completely unified theory of all the interactions in natrure, and its shortcomings are well recognized. Supersymmetry is a recent theoretical idea which represents a potentially significant addition to our current understanding of nature. It offers many promising avenues in the attempt to construct a unified field theory of physics, and alleviates many of the shortcomings of the standard model.

Supersymmetry has yet to be experimentally confirmed. Prompted by this fact, an experimental search for supersymmetric electrons and muons, produced in e^+e^- reactions at center of mass energies up to 61.4 GeV, was perfomed with the VENUS detector. The results of these searches are disscussed in the subsequent chapters. This chapter contains a disscussion of theoretical motivation for supersymmetry, begining with a description of the standard model, and midle with the phenomenolgy of the experimental signal used in these searches presented here. Finally, lepton production in two-photon process is discussed, since it makes dominant background which contaminates to supersymmetric particle search.

1.1 Standard model

Gauge symmetry is now believed to be a fundamental guiding priciple to determine the form of particle interactions. The strong, weak, and electromagnetic forces are

3

Fermions

Leptons			Quarks		
$\begin{pmatrix} \nu_e \\ e \end{pmatrix}_L$	$\begin{pmatrix} \nu_\mu \\ \mu \end{pmatrix}_L$	$\begin{pmatrix} \nu_\tau \\ \tau \end{pmatrix}_L$	$\begin{pmatrix} u \\ d' \end{pmatrix}_L$	$\begin{pmatrix} c \\ s' \end{pmatrix}_L$	$\begin{pmatrix} t \\ b' \end{pmatrix}_L$
——	——	——	u_R	c_R	t_R
e_R	μ_R	τ_R	d_R	s_R	b_R

Gauge bosons

EM	Weak	Strong
γ	Z^0 $W^\pm$	g_{ij}

Higss scalar H^0

Table 1.1: Fundamental particles in the standard model.

embedded in an $SU(3)_C \times SU(2)_L \times U(1)_Y$ gauge group. The color force is due to an $SU(3)_C$ color gauge group, with strong coupling constant, α_s. The electromagnetic and the weak forces are embedded in direct product of an $SU(2)_L$ weak isospin gauge group and a $U(1)_Y$ hypercharge gauge group. The electroweak force is governed by one coupling constant α_{EM}. The gauge groups predict the existence of four spin 1 gauge bosons: γ, Z^0, W^+, and W^-. These bosons are responsible for mediating the interactions between fermions. The non-Abelian nature of $SU(3)_C$ and $SU(2)_L$ gauge groups imply that these bosons can have self-interactions, unlike the photon in conventional QED. This is because the non-Abelian gauge bosons carry the same charge that they couple to, unlike Abelian gauge bosons such as the photon. Table. 1.1 shows fundamental particle spectrum in the stnadard model.

The strong force is carried by 8 gluons, which couple to color fields. Quarks are
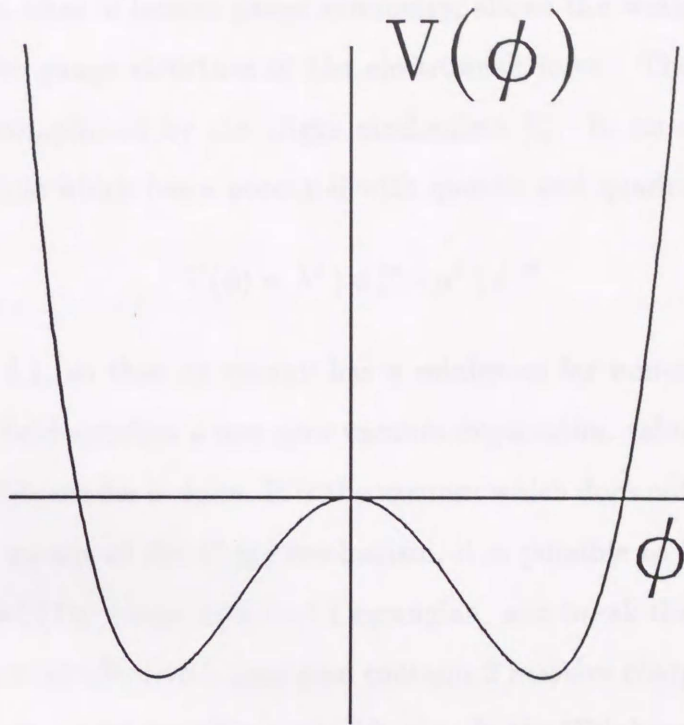
Figure 1.1: Higgs potential

The Higgs potential, $V(\phi) = \lambda^2 \mid \phi \mid^4 - \mu^2 \mid \phi \mid^2$, is shown here for non-zero μ, λ. The potential has a minimum at non-zero field value, $\mid < \phi > \mid = \sqrt{\mu^2/(2\lambda^2)}$. The Higgs potential always exhibits a degeneracy, as shown by the above double well. We have picked one possible solution for definiteness.

fermion filed which carry color, are found inside hadrons, and have fractional charge in units of 1/3 e. Hadrons which are consituted from 3 different colored quarks (baryon) or, one qurak and one anti-quark (meson), come in integer multiples of e and have no net color charge. The gluons are massless, and the force is infinitely ranged in a broken colored vacuum state. However, a broken colored vacuum can only exist inside hadrons, due to confinement. Quarks and gluons move relatively freely inside hadrons, since their force has the asymptotic freedom. The $SU(3)_C$ theory of the strong force predicts that free quarks and gluons can not be observed. This prediction must be experimentally verified. Forces between hadrons are carried by colorless objects such as pions instead of colored gluons. Thus gauge symmetry of the strong force is hidden at low energies.

The electromagnetic and weak forces are unified in the standard model, governed

by one coupling constant, α_{EM}, and one mixing angle, θ_W. A recently introduced theoretical idea, that of broken gauge symmetry, allows the weak bosons to acquire mass within the gauge structure of the electroweak force. The gauge symmetry breaking is accomplished by the Higgs mechanism [2]. In its simplest form, the Higgs is a particle which has a potential with quartic and quadratic terms,

$$V(\phi) = \lambda^2 \mid \phi \mid^4 - \mu^2 \mid \phi \mid^2,$$

shown in Fig. 1.1, so that its energy has a minimum for non-zero fields. In this way the Higgs field acquires a non-zero vacuum expectation value, about which the quantization of its modes is done. It is the vacuum which does not respect the gauge symmetry. By means of the Higgs mechanism, it is possible to begin with a manifestly $SU(2)_L \times U(1)_Y$ gauge invariant Lagrangian, and break the gauge symmetry, so that the resulting effective Lagrangian contains 2 massive charged bosons, 1 massive neutral boson, and 1 massless neutral boson. In the Weinberg-Salam model, the charged bosons arise from the raising and lowering operators of $SU(2)_L$ coupling to the vacuum expectation value of a Higgs doublet, while the massive neutral boson results from Higgs coupling to a mixture of the third component of weak isospin and hypercharge operators. This mixing is governed by the Weinberg angle. The orthogonal mixture obeyes a $U(1)_{EM}$ symmetry which the broken vacuum does obey, so that this boson is massless. The $U(1)_{EM}$ coupling is to the electric charge operator, which is given by the following linear combination:

$$Q = \frac{1}{2}(\sigma_3 + Y).$$

The massless boson which couples to above charge is the photon. The 3 massive bosons are the weak vector bosons, i.e., the W^+, W^-, and Z^0. The W bosons couple to weak isospin charge, which is only carried by left-handed fermions. The Z^0 couples to a combination of weak isospin charge and hypercharge. Since the vacuum expectation value of Higgs generates mass for all the weak bosons, weak force is short ranged. In contrast to this, the photon, being massless, has infinite range.

6

The weak force requires that fermions come in left-handed doublets, so that the left-handed electron and its neutrino belong to an isospin doublet. Since the right-handed electron is in an isospin singlet and it carries different quntum numbers than the left-handed electron. Therefore, the left-handed and right-handed electrons have different couplings to the Z^0, giving rise to interesting parity violating effects. Similar statements apply to other fermions in Table 1.1.

The standard model is completed by the two more features: the Higgs coupling to fermions, and KM matrix. The Higgs bosons have different Yukawa couplings to the different mass fermions. The KM matrix is an extension of Cabbibo angle to 3 generations of quarks.

1.2   Supersymmetry

Supersymmentry[3] is a very vital and new extension from the standard model. It postulates a symmetry between bosons and fermions, such that every ordinary bosons has a supersymmetric fermion partner, and every ordinary fermion has a supersymmetric bosonic partner. All supersymmetric particles have the identical gauge couplings as their partners, and, in an broken supersymmetry, the same mass. The gauge hierarchy problem is entirely alleviated in unbroken supersymmetry due to the perfect cancellation between fermion (boson) and superpartner boson (fermion) loop corrections. Since there are no known supersymmetric particles, supersymmetry must be broken. The radiative corrections to Higgs mass from virtual boson and fermion loops have oposite signs. Since the ordinary particles and their superpartners have the same couplings, the mass divergence are kept under finite value.

Realistic models of supersymmetry, with a plethora of new phenomena, have been extensively developed. Since no superpartners are yet known, the minimal supersymmetric extension of stnadrad model leads to doubling of the number of fields in Table 1.2. Note that the Higss sector has been enlarged to include two Higgs doublets. This is necessary since a single Higgs doublet can only generate masses for down-like quarks, i.e. those with charge -1/3 e, without destroying supersym-

Coventinal	Supersymmetric partners		
partcles	Weak eigenstates	Name	Spin
$\ell = e, \mu, \tau$	$\tilde{\ell}_L, \tilde{\ell}_R$	sclar leptons	0
$\nu = \nu_e, \nu_\mu, \nu_\tau$	$\tilde{\nu}$	scalar neutrinos	0
$q = u, d, s, c, b, t$	$\tilde{q}_L, \tilde{q}_R$	scalar quarks	0
g	$\tilde{g}$	gluinos	1/2
γ	$\tilde{\gamma}$	photino	1/2
Z^0	$\widetilde{Z^0}$	zino	1/2
$W^\pm$	$\widetilde{W^\pm}$	wino	1/2
$H^0_{1,2}, H^\pm_{1,2}$	$\widetilde{H^0_{1,2}}, \widetilde{H^\pm_{1,2}}$	higgsino	1/2

Table 1.2: Supersymmetric particle spectrum

metry. It should be pointed out that Table 1.2 lists the particle spectrum before supersymmetry is broken. This means that the final mass eigenstates may involve mixing between the orginal weak eigenstates. Because such mixing involves details of the model used to the generate symmetry breaking, few general statements can be made. Experimental searches, such as the one presented here, must typically make very restricted assumptions about the model they are testing, since the experimental signatures often depend upon the details of the model, such as mixing.

Many phenomenological models of supersymmetry introduce a new quantum number, R, which is multiplicatively conserved. All ordinary particles have R= +1, while their superpartners have R= −1. R-parity can be broken by non-zero vacuum expectation values for some neutral scalar superpartner, such as the scalar neutrino, but this would lead to lepton number non-conservation. For instance, the process $\tilde{\nu} \to \nu + \gamma$ would be allowed if R-parity were violated. Although strong R-parity violation can be ruled out by lepton number conservation at low energies, weak R-parity violation is allowed. This is mentioned here because, although R conservation is virtually safe in accelerator experiments, but weak R-parity violation might be very significant in early cosmology.

R-parity conservation has several implications. It implies that superpartners must be created or destroyed in even numbers. Thus, accelerator experments must
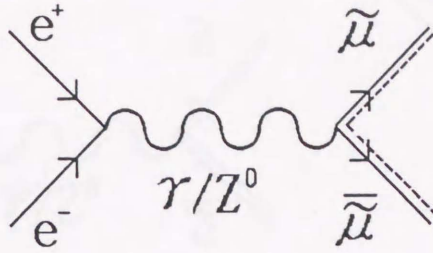
Figure 1.2: Feynman diagram for scalar muon pair production in e^+e^- reactions

have energies large enough to be able to produce at least two superpartners in a collision process. Then, once a superpartner is created, it always decays to another lighter superpartner. This process ends up with the lightest superpartner (LSP), which is absolutely stable. If LSP were charged, or had strong interactions, its relics from the big bang would have condensed into galaxies in the form of heavy isotopes. Terrestrial searches have exclueded such heavy isotopes to less than that expected from usual big bang scenario. Thus, LSP must be neutral, and is often assumed to be the photino (or a mixture of the photino and higgsino).

The weak force distinguishes left-handed particles from right-handed particles. Therfore each quark and lepton has two superpartners, $(\tilde{q}_L, \tilde{q}_R)$ and $(\tilde{\ell}_L$ and $\tilde{\ell}_R)$, each corresponding to the two chirality states of the fermion. Neutrinos have one partner in the standard model where they have only left-handed components. Since a small contribution of Z^0 exchange in our energy region and ambiguous $\widetilde{Z^0}$ contribution [5], the cross section of superpartner production in this thesis is given only by the contribution of QED. The weak eigenstates make no sense as mass eigenstates, and we treat mass eigenstates $\tilde{\ell}_1$ and $\tilde{\ell}_2$ which are mixing states of $\tilde{\ell}_L$ and $\tilde{\ell}_R$.

The Feynman diagram for scalar muon pair production from e^+e^- reaction is presented in Fig. 1.2. The differential cross section is given by

$$\frac{d\sigma}{d\Omega} = \frac{\alpha^2}{8s}\beta^3 \sin^2\theta$$

in a case of large mass splitting [6], $m_{\tilde{\mu}_1} \ll m_{\tilde{\mu}_2}$, where β is the velocity of the produced scalars and α is the QED coupling constant. For the degenerate case,

9

(a)   (b)
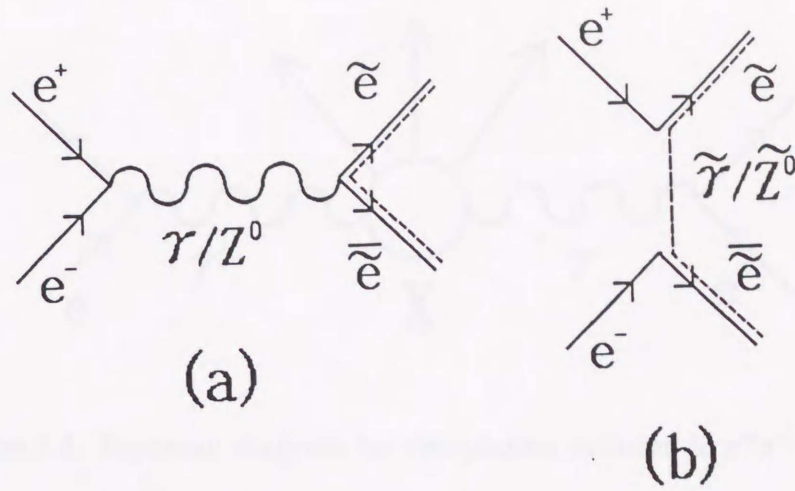
Figure 1.3: Feynman diagrams for scalar electron pair production in e^+e^- reactions

$m_{\tilde{\mu}_1} = m_{\tilde{\mu}_2}$, the differential cross section is to be multiplied by 2.

The Feynman diagrams for scalar electron pair production in e^+e^- reaction is presented in Fig. 1.3. Contributions from t-channel photino exchange are added to that of the muon production diagram. In the case of the large mass splitting, only the process, $e^+e^- \rightarrow \tilde{e}_1\bar{\tilde{e}}_1$ contributes. Differntial cross section [7] is now

$$\frac{d\sigma}{d\Omega} = \frac{\alpha^2}{4s}\beta^3 \sin^2\theta\{1 + (1 - \frac{4}{1 - 2\beta\cos\theta + \beta^2 + \mu^2})^2\},$$

where $\mu = 2m_{\tilde{\gamma}}/\sqrt{s}$. In the degenerate mass case, the processes, $e^+e^- \rightarrow \tilde{e}_2\bar{\tilde{e}}_2$, $e^+e^- \rightarrow \tilde{e}_1\bar{\tilde{e}}_2$, and $e^+e^- \rightarrow \tilde{e}_2\bar{\tilde{e}}_1$ are possible and the resulting cross section is given by

$$\frac{d\sigma}{d\Omega} = \frac{\alpha^2}{8s}[\beta^3 \sin^2\theta\{1 + (1 - \frac{4}{1 - 2\beta\cos\theta + \beta^2 + \mu^2})^2\} + \frac{16\mu^2\beta}{(1 - 2\beta\cos\theta + \beta^2 + \mu^2)^2}].$$

An assumption that the photino is LSP allows us to make several experimental statements for the photino interactions with matter. Photinos can interact with bulk matter via t-channel exchange of quarks or scalar quarks, or by the s-channel fusion of the photino and quark and into scalar quark. Numerically the cross section [8] is of order of that for neutrino interactions with bulk matter. Thus collider experiments may regard photinos as non-interacting partilcles and the most prominent signal of

10
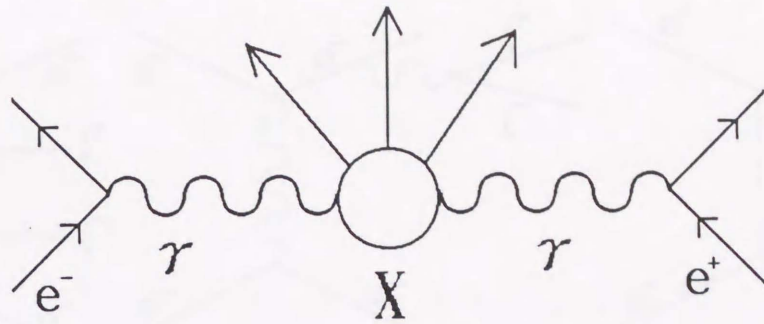
Figure 1.4: Feynman diagram for two-photon collision in e⁺e⁻ collision

superpartner production will be manifested in missing energy which is carried off by the escaping photinos.

On the other hand, if photino is heavier than scalar lepton and all superpartner particles lighter than scalar lepton interact only weakly with scalar lepton, the produced scalar lepton may have a long life time and could be observed as stable particles. In this case a search is also possible by looking for the pair production of stable scalar particles.

1.3 Two-photon process

Feynman diagram for two-photon process is shown in Fig. 1.4. Although this diagram is of higher order in the QED coupling constant than the process due to single photon exchange, the cross section for two-photon process can be very large, because single-photon exchange requires a spacelike photon with a mass equal to the center-of-mass energy, while the two-photon process proceeds with timelike photons of generally lower energy as well as of very low mass. Thus the two-photon process favors the production of state X which has much lower energy than that of single-photon exchange. In the e⁺e⁻ reaction, the electron beams act essentially as intense sources of bremsstrahlung radiation and this implies that there occurs the collisions of high energy photon with a rather large probability.

Fig. 1.5 shows diagrams of the leading-order (α^4) which contribute to the process

11
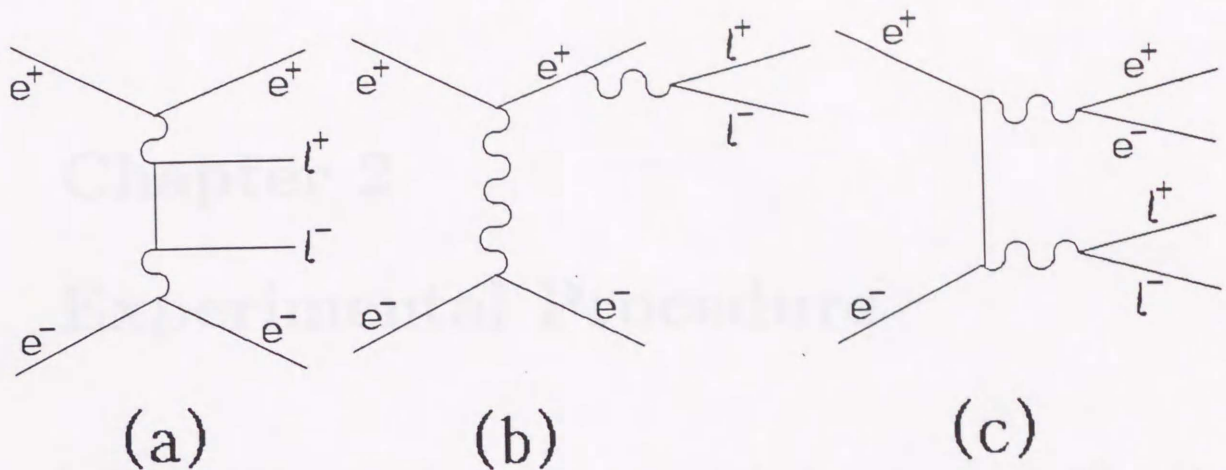
Figure 1.5: Feynman diagrams contributing to the reaction $e^+e^- \rightarrow e^+e^-\ell^+\ell^-$. (a) multiperipheral, (b) single photon conversion, (c) double conversion.

$e^+e^- \rightarrow e^+e^-e^+e^-$ and $e^+e^- \rightarrow e^+e^-\mu^+\mu^-$. When all possible permutations are made, there are a total of thirty-six amplitudes for four-electron final state and twelve for the $e^+e^-\mu^+\mu^-$ one, all of which must be summed together in each case before taking the absolute square to calculate the cross section. It is prohibitively difficult to carry out exactly such a calculation and reduce the result analytically to a manageable expression, so that in practical calculations the amplitudes are summed numerically before squaring. This makes the algebra more straightfoward, but care must be taken to avoid numerical instabilities.

The full leading-order calculation for both processes has been done with Monte Carlo integration by Berends, Daverveldt, and Kleiss[4]. Their calculations demonstrate that, for the experimental situation where only two of the leptons pass through the barrel detector, the first digram in Fig. 1.5 (commonly called the *multiperipheral* diagrams) completely dominates the cross section. In other word, untagged experiments, in which both of scattered electron and positron can not been detected and only the produce lepton-pair can been detected, are sensitive only to the multiperipheral diagrams. These diagrams are important to two-photon physics because they represent the interactions between two photons each of which has been radiated by the opposing beam in the collider.

Chapter 2

Experimental Procedure

In this chapter we give a detailed description of the electron-positron collider and the detector system which are employed in the present experiment.

2.1   TRISTAN Accelerator

TRISTAN (<u>T</u>ransprposable <u>R</u>ing <u>I</u>ntersecting <u>ST</u>orage <u>A</u>ccelerator in <u>N</u>ippon) [9] is an e^+e^- colliding beam accelerator operated at the center-of-mass energies around 60 GeV at the National Laboratory for High Energy Physics (KEK). Fig. 2.1 shows a layout of the TRISTAN accelerator. The main storage ring has a size of 3018 m in circumference and has four straight sections of 193 m long where experimental halls and accelerating RF cavities are located. The RF cavities consist of normal type ones and super-conducting ones.

Electrons and positrons are first accelerated up to 2.5 GeV by a linear accelerator of 400 m long and are accumulated into an accumulation ring. The beams are accelerated there to 7.5 GeV and injected into the main ring. Two electron bunches and two positrons bunches are stored in the main ring and accelerated up to the maximum beam energy. The total beam current is more than 12 mA at maximum and the beam life time is 1.5-2.5 hours.

In Nov. 1986 the TRISTAN was completed and came into operation at the beam energy of 25.0 GeV. The super-conducting RF cavities were installed in Oct.1988 and the beam energy rose to 30 GeV and maximum total beam current was 10 mA. In the Summer of 1989, the maximum center-of-mass energy was 61.4 GeV,
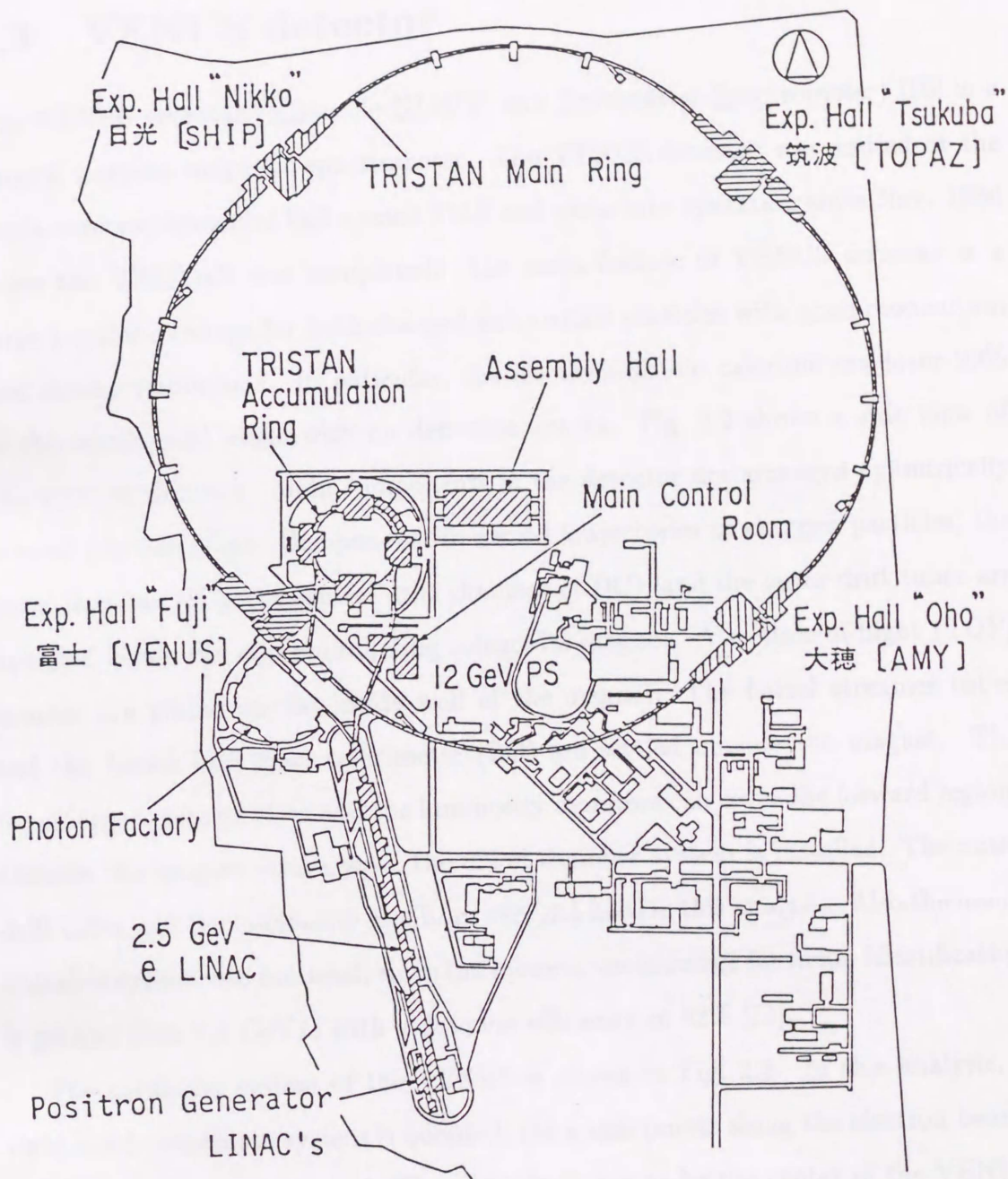
Figure 2.1: TRISTAN accelerator
Our VENUS detector has been settled in south-west experimental hall named FUJI.

the peak luminosity amounted to $6 \times 30^{30} \text{cm}^{-2}\text{s}^{-1}$ and average luminosity was $0.9 \times 10^{30} \text{cm}^{-2}\text{s}^{-1}$.

2.2   VENUS detector

The VENUS detector (VErsatile NLHEP and Universities Spectrometer) [10] is a general purpose magnetic spectrometer. The VENUS detector was settled at the south-west experimental hall named FUJI and came into operation since Nov. 1986 when the TRISTAN was completed. The main feature of VENUS detector is a large angular coverage for both charged and neutral particles with good momentum and energy resolutions. In paticular, the electromagnetic calorimeters cover 99% of the whole solid angle with no detection cracks. Fig. 2.2 shows a side view of the VENUS detector. Main components of the detector are arranged cylindrically around the beam-line. Components to record trajectories of charged particles, the inner chamber (IC), the central drift chamber (CDC), and the outer drift tubes are installed inside the superconducting solenoidal magnet. Also time-of-flight (TOF) counter are placed on the inside wall of the magnet. The barrel streamer tubes and the barrel lead glass calorimeter (LG) are settled outside the magnet. The liquid-argon counter (LA) and the luminosity monitors can cover the forward region. Outside the magnet return yoke, the muon chamber system is installed. The outer drift tubes and the luminosity monitors were not used in this analysis. Also the muon chmaber system was not used, since the momentum coverage for muon identification is greater than 2.3 GeV/c with a detction efficiency of 92% [11].

The cordinate system of the VENUS is shown in Fig. 2.3. In this analysis, a right-hand coordinate system is adopted; the z axis points along the electron beam, and the y axis points upward. The orgin is chosen to be the center of the VENUS detector where e^+ and e^- collide.

2.2.1   Beam pipe

The beam pipe made of aluminum has an inner radius of 90 mm in the central region of $\mid z \mid < 135$cm. In the interaction region of $\mid z \mid < 25$cm, the thickness of the beam
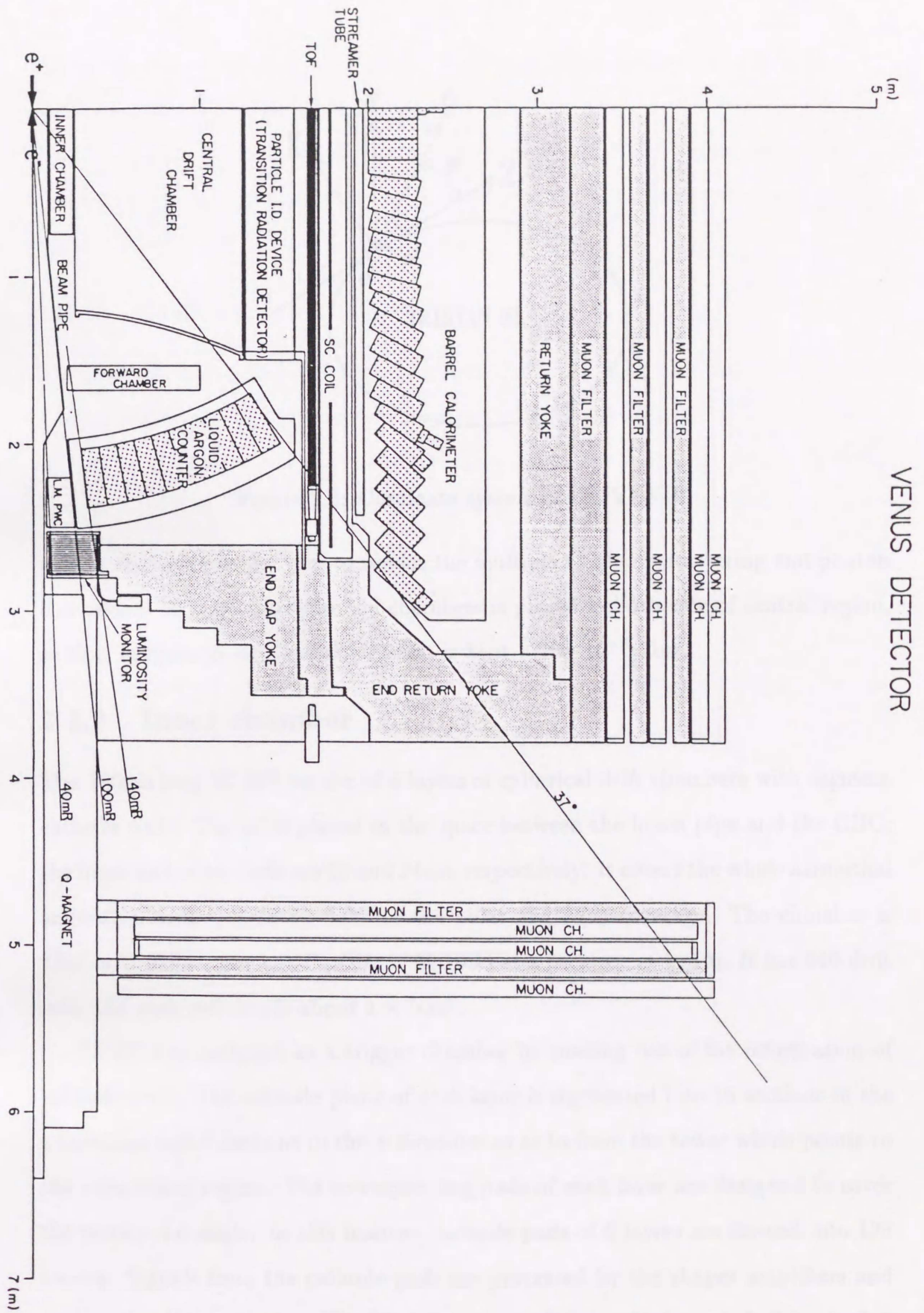
Figure 2.2: Side view of VENUS detector

16
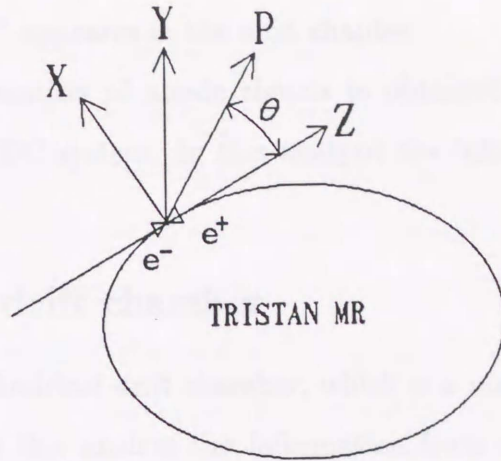
Figure 2.3: Cordinate system of the VENUS

pipe is chosen to be 2.5 mm to reduce the multiple Coulomb scattering and photon conversion. A pair of vacuum ion chambers is placed in both side of central region, so that vacuum at the interation point is kept below 10^{-8} Torr.

2.2.2 Inner chamber

The 160cm long IC [12] consits of 6 layers of cylinrical drift chambers with segment cathode pads. The IC is placed in the space between the beam pipe and the CDC; the inner and outer radii are 10 and 24cm, respectively. It covers the whole azimuthal angle (ϕ), while $|\cos\theta| < 0.96$ for the polar angle (θ) coverage. The chmaber is filled with HRS gas ($Ar:CO_2:CH_4 = 89:10:1$) at a pressure of 1 atm. It has 640 drift cells and each sell size is about $1 \times 1 cm^2$.

Th IC was designed as a trigger chamber by making use of hit information of cathode pads. The cathode plane of each layer is segmented into 16 sections in the z direction and 8 sections in the ϕ direction so as to form the tower which points to the interaction region. The corresponding pads of each layer are designed to cover the same solid angle. In this manner, cathode pads of 6 layers are formed into 128 towers. Signals from the cathode pads are processed by the shaper amplifiers and sent to the discriminators. The hit information of the cathode pads is fed into fast track-finding processors (TF-IC). The TF-IC searches charged tracks starting from

17

the interaction point in the r-z plane. A detailed description of z trigger used by the IC and the TF-IC appeares in the next chapter.

The timing information of anode signals is obtained by using the amplifier-discriminators and TDC system. In this analysis the information of anode signals was not used.

2.2.3   Central drift chamber

The CDC[13] is a cylindrical drift chamber, which is a main tracking device of the VENUS detector. In this analsys the information from only the CDC were used in determing charged particle momenta. The dimension is 300 cm long with inner and outer radii of 25 and 126 cm, respectively. It consists of 20 layers of axial wires parallel to the beam axis and 9 layers of slant wires at angles of $\pm 3.5°$. It has 7104 drift cells and its cell size is about $2 \times 2 \text{cm}^2$. Two adjacent layers of axial wires are staggered by a half cell. The chamber is filled with HRS gas at a pressure of 1atm.

Signals from anode wires are processed by the preamplifiers [14], and sent to the postamplifier-discriminators. The drift time is measured by using TDC system [15] on FASTBUS. Signals from discriminators are also fed into the fast track-finding processors (TF-CDC) [16] on FASTBUS. The TF-CDC searches charged tracks in the r-ϕ plane. A detailed description of r-ϕ trigger used by the CDC and the TF-CDC is given in the next chapter.

For charged tracks in the polar angle range $| \cos\theta | < 0.75$, twenty sets of r-ϕ and nine sets of r-z coordinates are measured. The mean spatial resolution is 270μm on r-ϕ and 6.3mm on r-z. The momentum resolution of charged particles in the plane transverse to the beam axis is $\sigma_p/p = \sqrt{(0.8p_t)^2 + 1.2^2}\%$, at B=7.5kGauss, where p_t is transverse momentum expressed in GeV/c. The angular resolutions in azimuthal and polar angles for charged particles of high momenta are $\sigma_\phi \approx 1.3$ mrad and $\sigma_\theta \approx 9 \times \sin^2\theta$ mrad respectively.

2.2.4 Time-of-flight counters

The TOF counter measures time-of-flight for charged particle and the timing from e^+e^- collision. Then the particle velocity is obtained from the path length of the track recognized by the CDC and the mass of the charged particle is calculated. The cosmic-ray events can be rejected by timing measurement. The TOF counter [17] consists of 96 plastic scintillators of 466cm long surrounding the outer drift tubes at a radius of 1.66m just inside the superconducting magnet. Since there are 3mm gaps between adjacent counters, they causes an inefficiency for high momentum charged tracks. Each scintillation counter is viewed from the both ends with the phototubes through long acrylic light guides.

The output signal of each phototube is processed through the discriminator with signal threshold, the charge sensitive ADC [18] and the high resolution TDC [19] in order to obtain both timing and pulse hight information. Output signals from discriminators are also used for the event trigger. The pulse hight information is mainly used to correct the timing slewing.

The time-of-flight of each charged particles is calculated by using information from phototunes on both sides of the counter. The timing resolution is 200ps for Bhabha and muon-pair events. The position resolution in z direction is 4cm.

2.2.5 Superconducting solenoidal magnet

The superconducting solenoidal magnet [20] provides a uniform magnetic field of 7.5kGauss in the direction of z axis in order to measure charged particle momentum. The dimension of the magnet is 3.4m in diameter and 5.2m in length. The magnetic field was measured before detector installation and found to be uniform within 1% throughout the tracking volume. The effective thickness of this magnet is chosen to be 0.64 radiation lengths to reduce the production probability of electromagnetic components.

2.2.6 Barrel lead glass calorimeter

The barrel electromagnetic calorimeter [21] consisting of 5160 lead glass modules is located outside the solenoidal magnet for measuring energies of photons and electrons. It has an polar angle coverage of $| \cos \theta | < 0.80$ and is divided into 120 segments in the ϕ direction and 43 segments in the z direction. The lead glass modules are placed in an semi-tower geometry with which each module approximately points to the interaction point. It tilts at small angle in both ϕ and z directions in order to avoid the large shower leakage along inter-module gaps. The lead-glass modules are made of NIKON DF6 with a reflection index of 1.8. Its typical size is $12.0 \times 11.6 \text{cm}^2$ in cross section and 30cm in length corresponding 18 radiation lengths ($X_0 = 1.7$cm). A phototube surrounded by μ-metal magnetic shield is mounted on each module together with a plastic light guide of 5 cm long. For monitoring the gain variation of phototubes, light pulses from Xenon flash tubes are distributed to each phototube through optical fibers.

Signals from phototubes are sent to the 96 channel charge integrating ADC. For the enery trigger, the LG calorimeter is grouped into 58 segments: 7 segments in the z direction and 8 segments in the ϕ direction. Analog signals in each ADC module corresponding to one segment of the calrolimeter are summed up into one segment-sum signal. Each segment-sum signal is fed to a discriminator and its output signal is used for segment-sum trigger. Morever, all 58 segment-sum signals are sent to analog-sum circuit in order to get total energy deposit in the barrel calroimeter, used for the total-energy trigger.

The energy resolution is $\sigma_E/E = 7.0/\sqrt{E} + 2.4$ %[22], where E in units of GeV, and the angular resolutions of shower center are $\sigma_\phi = 4$mrad and $\sigma_\theta = 4$mrad for Bhabha events at E = 28 GeV.

2.2.7 End-cap liquid argon calorimeter

Two LA calorimeters for measuring the energies of photons and electrons are placed between the CDC and both endcaps of the magnetic return yoke. Each calorimeter consists of 480 tower modules which are approximately pointing to the interaction

point and covers 0.79<| $\cos\theta$ |<0.99. One tower has a depth corresponding 20.5 radiation lengths and consists of 71 calcium-Pb plates of 1.5 mm thick. The whole calorimeter is filled by liquid argon of 86°K. An average granularity is about 2.9° × 2.9°.

Lead plates of each module are electrically segmented into four groups. Accordingly, each side of the calorimeters has 1920 channels of signal readouts. Signals from lead plates are fed to preamplifiers and then sent to the shape amplifires and pulse hights are processed by the sample-hold ADC's. Two types of energy sum triggers are provided using the analog sum circuits for end-cap calorimeters. Each calorimeter is divided into 12 sectors and each sector is further divided into the inner part (0.91 <| $\cos\theta$ |< 0.99) and the outer part (0.79 <| $\cos\theta$ |< 0.91). Thus energy sum signals of each subsector provide totally 24 sector sum triggers. Furthermore, the total sum signal of all 1920 channels for each side is provided.

The energy resolution is σ_E =3.5% for Bhabha events at E=28GeV and $\sigma_E =$ $11.3/\sqrt{E}+1.4$ %, where E in units of GeV. The angular resolutions of shower center are $\sigma_\phi = 6$mrad and $\sigma_\theta = 4$mrad for Bhabha events.

2.2.8 Luminosity monitor

In order to measure small angle Bhabha events, a pair of luminosity monitors (LM) [23] is placed surrounding the beam pipe at 155 cm apart from the interaction point. The luminosity monitor consists of 27 alternating layers of lead sheets and plastic scintillators corresponding to 20 radiation length in total. It is divided into 8 sectors in the r-ϕ plane. The angular coverage is between 76 and 137 mrad. Scintillation lights are guided to wavelength shifters through inner and outer edges of the scintillators, and then transmitted to the mesh type phototubes. Pulse hights of phototube signal are measured by the charge sensitive ADC's. In this analysis the information form the LM is not used.

21

2.2.9 Event trigger

There are two levels of event triggers in the VENUS trigger system: First-level trigger which determines the trigger in every crossing and second-level trigger which processes after the first level trigger is fired. A detailed description of event triggers appears in the next chapter.

2.2.10 Data acquisition system

As shown in Fig. 2.4, the data acquisition system of the VENUS detector has tree structure. Signals from the front-end electronics are digitized by FASTBUS, CAMAC and TKO modules. All together, there consist of 25k channels. All data are transferred to FASTBUS memory buffers and collected by 68K20FPI CPU module [24] on FASTBUS which consists of 68020 microprocessors and 1Mword buffered memory. Then all data in 68k20FPI are read by an on-line computer VAX11/780 through the FASTBUS-VAX interface [25]. A typical data size is about 5k bytes per event and it takes about 20 ms to read the data into the VAX11/780. The dead time is typically 10%. The collected data are transferred to the main computer, FACOM M780, via optical link and then stored on the automatic loading cartridge tape library. The VAX11/780 is also linked another on-line computer VAX8530 and the collected data are quickly analyzed to check the run status.

The VENUS data acquisition system has a special feature called *fast clear scheme*. Since the the beam crossing occurs every 5μs (under 2-bunch per each electron and positron operation), sample-and-hold of front-end analog signals and/or analog-to-digital conversion are performed for every beam crossing. If any event trigger conditions are not satisfied, a fast clear signal is generated at 800ns before the next beam crossing. By receiving the fast clear signal, all front-end modules reset their sample-and-hold circuits and are ready for next event. If the trigger conditions are satisfied, analog-to-digital conversion for sample-and-hold signals, data compression, and data transfer proceed. Careful design and construction were done for the most of the front-end electronics to provide a good resolution and stability.

Figure 2.4: Data acquision system of the VENUS

Chapter 3
Trigger system

In e^+e^- colliding-beam experiments, a large number of readout channels for detector signals have to be handled. At the TRISTAN, electron and positron collide every $5\mu s$ and the detectors do not have to miss any physically significant signals. As the cross section of the processes which we aim to analyze is of order of $\sim$pb to $\sim$nb, the corresponding event rate is less than 1 event/minute. Most of events are background due to beam-gas, beam-beam pipe, and cosmic-ray events. The trigger system is expected to reject most of these backgrounds while not to miss the true events. All events happened at every beam crossing are collected after appropriate filtering and stored in certain memory devices. Of course the data storage rate is required to be as low as possible from a finite capability of the data aquisition system.

For the superpartner search, the event trigger is requied to accept acoplanar charged-pair event with low transverse momenta. The muon-pair events do not deposit so much energy into the LG calorimeter and hence the event trigger has to be decided from the information of tracking devices. However the backgrounds due to beam-gas and beam-beam pipe events contribute mainly to the low mometum region and the trigger rate is influenced by the beam condition.

There are two levels in VENUS event trigger system. The first-level event trigger decides the trigger on every $5\mu s$ and then requires the data collection to online computer VAX11/780 or 68K20FPI microprocessor module on FASTBUS. The 68K20FPI module was also used as a processor for the second-level. The event trigger in the second-level is defined on the basis of the data collected with the first-level trigger. The second-level trigger demands the data collection to the on-
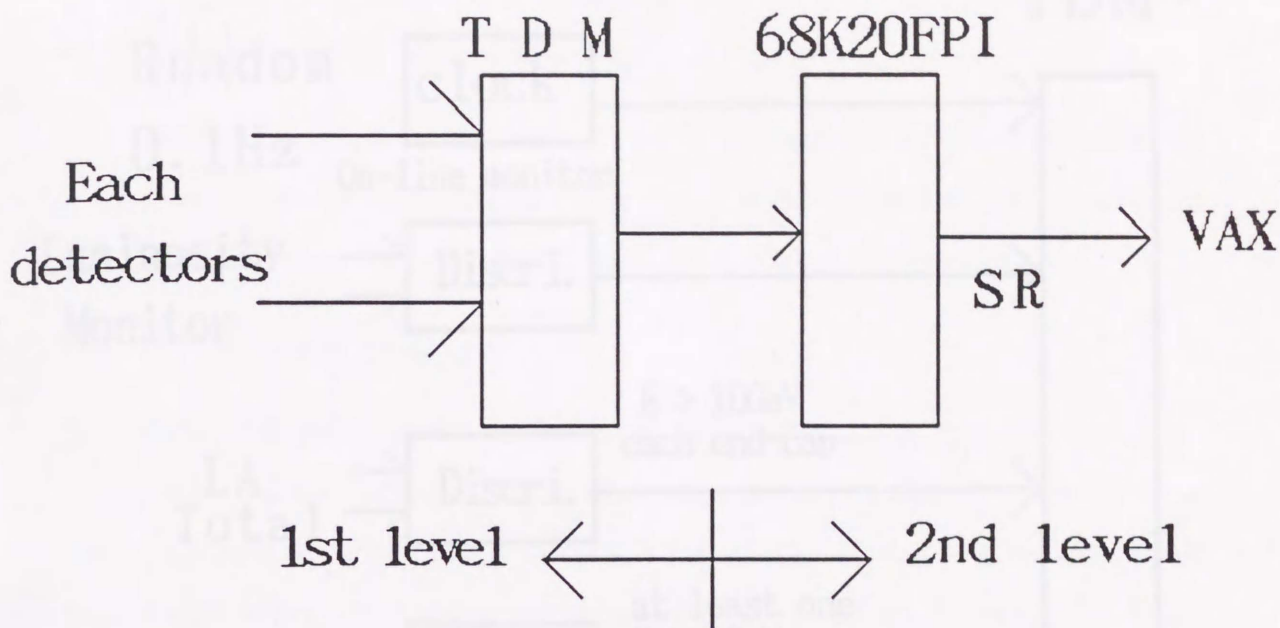
Figure 3.1: Schematic view of trigger system of VENUS, which consists of two-level.

line computer VAX11/780. The second-level trigger has been employed since Dec. 1989. Fig. 3.1 shows a schematic view of two level trigger system of the VENUS. All trigger signals from the first-level trigger are sent to the trigger decision module (TDM) on FASBUS and then the TDM demands a computer interrupt to enable the second-level trigger or immediately to collect the event data.

3.1 First-level trigger

There are two types of event triggers in the first-level trigger of the VENUS trigger system [26]: one is neutral triggers on the basis of the information of energies from calorimeters and the other is charged-track triggers defined by the information from tracking devices. The neutral trigger and the charged trigger are used complemetarilly for redundancy of event triggering. Fig. 3.2 shows a block diagram of the first-level trigger system in the VENUS. In addition, a periodical trigger other than the above event triggers is employed at a rate of 0.1 Hz in order to monitor the status of detectors.

The efficiency of the event trigger is estimated in the following way:

1. We select those events which are collected by the complementary trigger. For
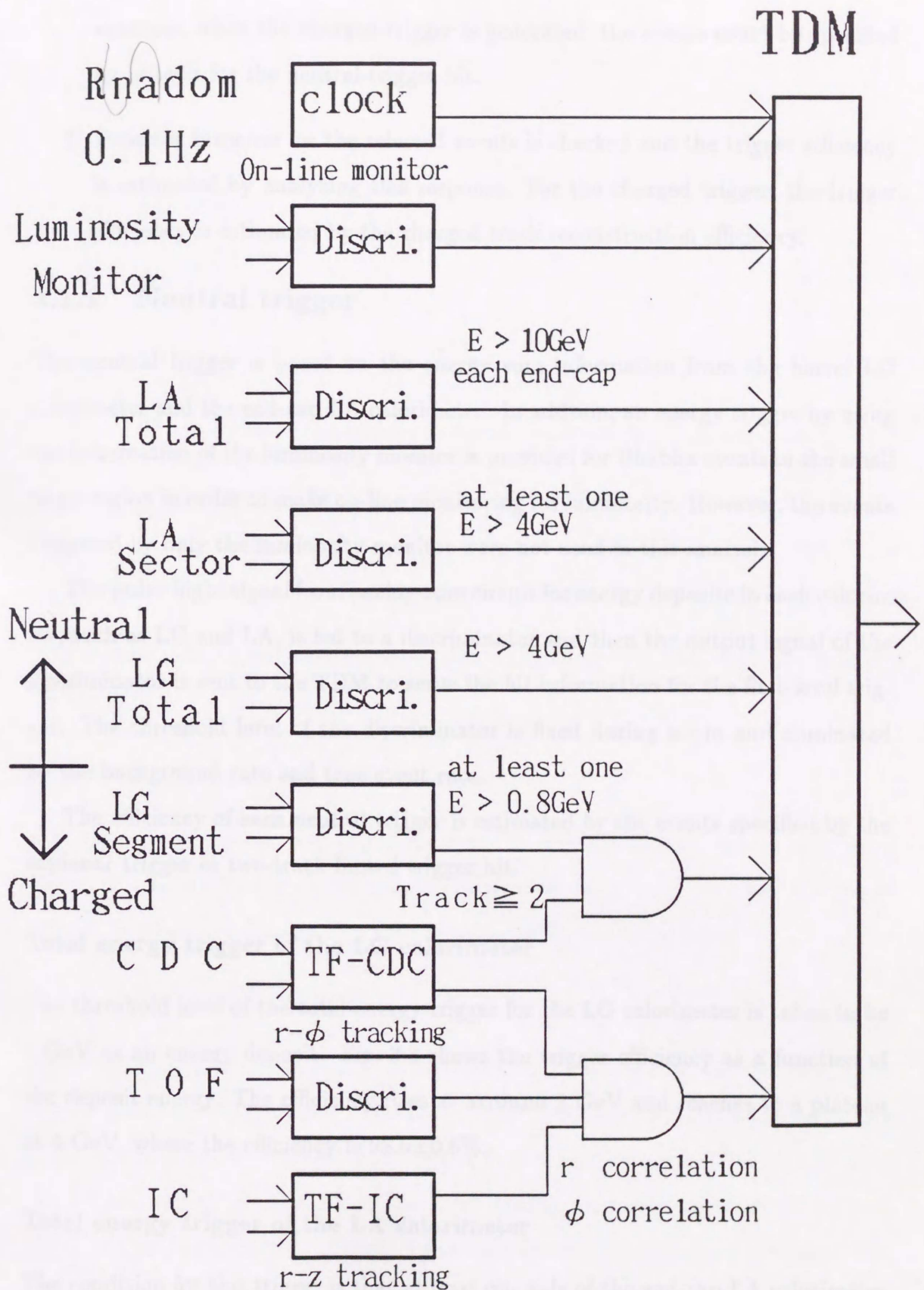
Figure 3.2: Schematic view of fisrt level trigger

example, when the charged-trigger is generated, the events could be specified by criteria for the neutral-trigger hit.

2. Detector response for the selected events is checked and the trigger efficiency is estimated by analyzing this response. For the charged trigger, the trigger efficiency is estimated by the charged track reconstruction efficiency.

3.1.1　Neutral trigger

The neutral trigger is based on the energy sum information from the barrel LG calorimeter and the end-cap LA calorimeter. In addtion, an energy trigger by using the information of the luminosity monitor is provided for Bhabha events in the small angle region in order to make on-line monitoring for luminosity. However, the events triggered by only the luminosity monitor were not used in this analysis.

The pulse-hight signal from analog-sum circuit for energy deposite in each calorimeter, such as LG and LA, is fed to a discriminator and then the output signal of the discriminator is sent to the TDM to serve the hit information for the first-level trigger. The threshold level of the discriminator is fixed during a run and dominated by the background rate and true event rate.

The efficiency of each neutral trigger is estimated by the events specified by the coplanar trigger or two-track limted trigger hit.

Total energy trigger of the LG calorimeter

The threshold level of the total energy trigger for the LG calorimeter is taken to be 4 GeV as an energy deposit. Fig. 3.3 shows the trigger efficiency as a function of the deposit energy. The efficiency rises at arround 2 GeV and reaches to a plateau at 4 GeV, where the efficiency is 98.6±0.6%.

Total energy trigger of the LA calorimeter

The condition for this trigger is that at least one side of the end-cap LA calorimeter has total energy deposit larger than 6GeV. Fig. 3.4 shows the trigger efficiency as
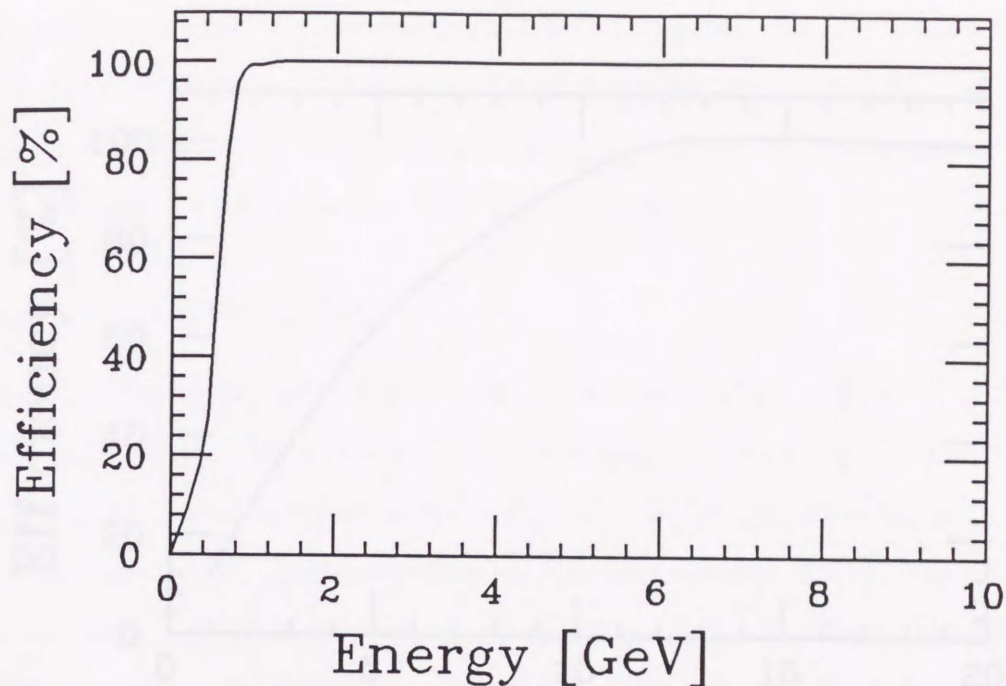
Figure 3.3: Efficeincy of the total energy trigger of the LG calorimeter

a function of the deposit energy. It reaches a plateau at 12 GeV with an efficiency 99.5±0.2%.

Sector sum trigger of the LA calorimeter

For the LA calorimeter, any one of its sector is required to have energy deposit of larger than 2.5GeV. Fig. 3.5 shows the trigger efficiency as a function of deposit energy. It reaches a plateau at 4 GeV with an efficiency 99.5±0.5%.

3.1.2 Charged trigger

The charged trigger is based on the information from tracking devices, the IC in the r-z plane, the CDC in the r-ϕ plane and the TOF counters. In addition to the track infromation, the segment sum signals in the LG are used. The signals from the IC and the CDC are send to the track-finding modules (called as TF-IC and TF-CDC, respectively) on FASTBUS and then these TF's find charged tracks. The TF's have a programable look-up table of hit patterns induced by charged tracks originating from the interaction point. A detailed description of the present look-up table method is expressed in Appendix A. The two-track limited (TTL) trigger and
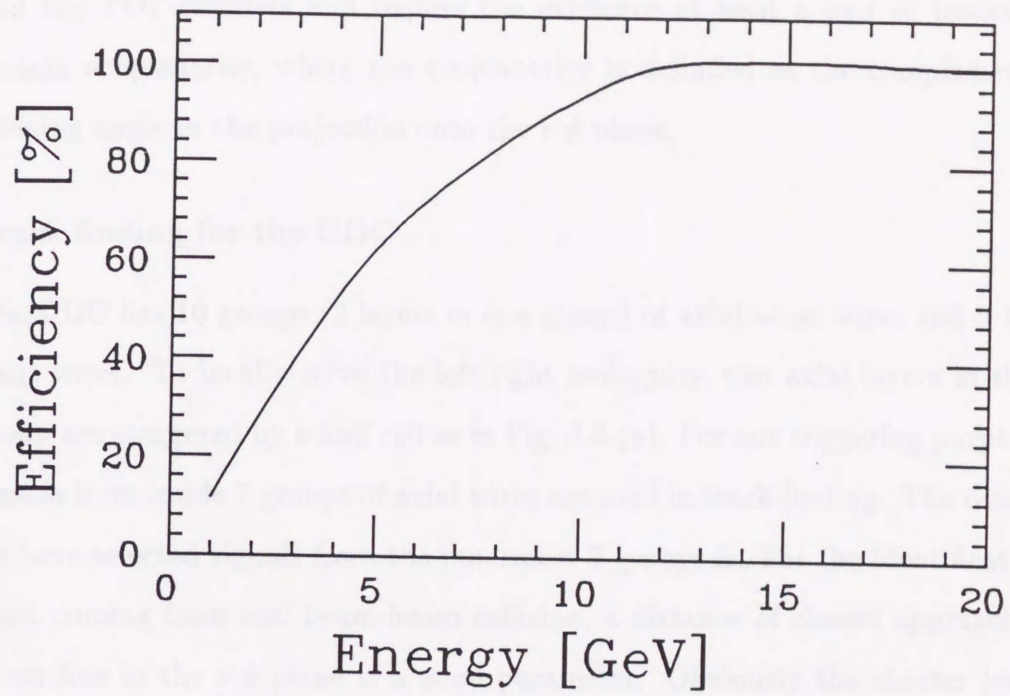
Figure 3.4: Efficiency of the total energy trigger of the LA calorimeter
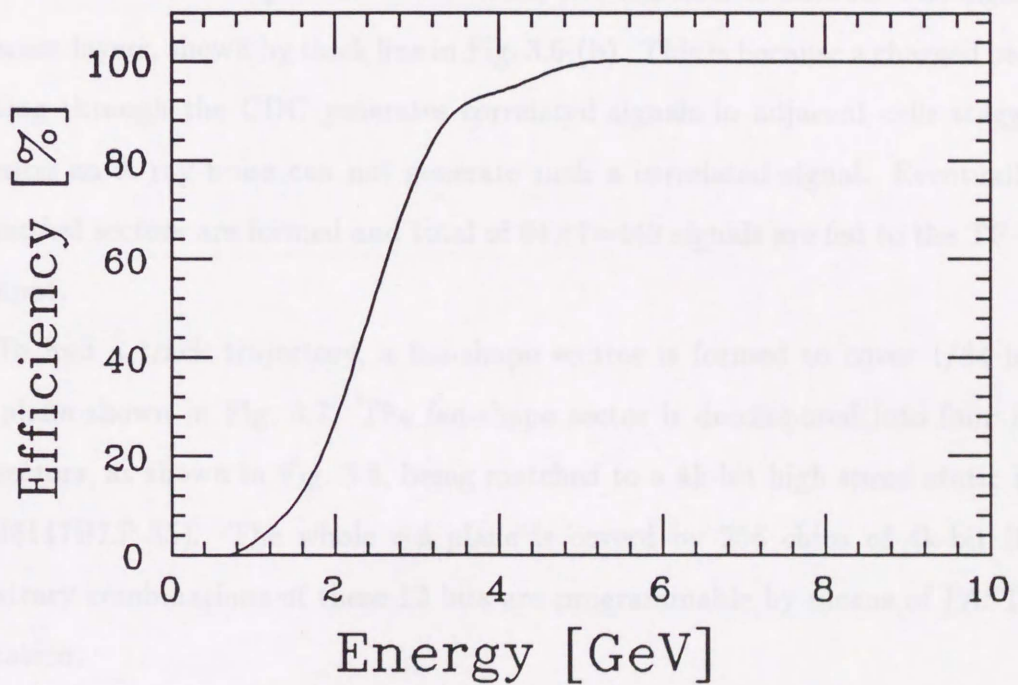
Figure 3.5: Efficeincy of the sector sum trigger of the LA calorimeter

the coplanar trigger use the geometrical knowledge from the TF-IC, the TF-CDC and the TOF-counters and require the existence at least a pair of tracks with a certain acoplanarity, where the acoplanarity is definded as the complement of an opening angle in the projection onto the r-ϕ plane.

Track finding for the CDC

The CDC has 10 groups (2 layers in one group) of axial sense wires and 9 layers of slant wires. To locally solve the left-right ambiguity, two axial layers in the same group are staggered by a half cell as in Fig. 3.6-(a). For our triggering purpose, only signals from inside 7 groups of axial wires are used in track finding. The reason why we have selected signals from the innermost 7 groups is: For the identification of a track coming from real beam-beam collision, a distance of closest approach to the beam line in the r-ϕ plane is a good parameter. Obviously the shorter lever arm gives the better resolution distance to determine the closet approach. In addition , inner groups can cover a wider angular region for a large acceptance for processes of interest. In order to reject the X-ray noise, the coincidence between two signals in adjacent layers, shown by thick line in Fig. 3.6-(b). This is because a charged particle passing through the CDC generates correlated signals in adjacent cells staggered, whereas an X-ray noise can not generate such a correlated signal. Eventually, 64 azimuthal sectors are formed and total of $64 \times 7 = 448$ signals are fed to the TF-CDC as input.

To find a track trajectory, a fan-shape sectror is formed to cover 1/64 in the r-ϕ plane shown in Fig. 3.7. The fan-shape sector is decomposed into four 12-bit subsectors, as shown in Fig. 3.8, being matched to a 4k-bit high speed static RAM (HM6147HLP-35). The whole r-ϕ plane is coverd by 256 chips of 4k-bit RAM. Arbitrary combinations of these 12 bits are programmable by means of FASTBUS operation.

The basic hit patterns are generated on the subsector by simulated tracks originating from the interaction point. By taking account of the inefficiency of chamber cell, a pattern which any one or two cells are missing in the 7 layers should be allowed
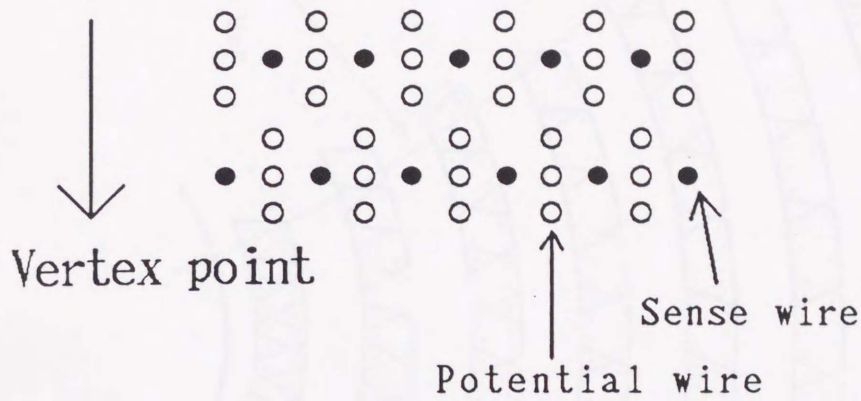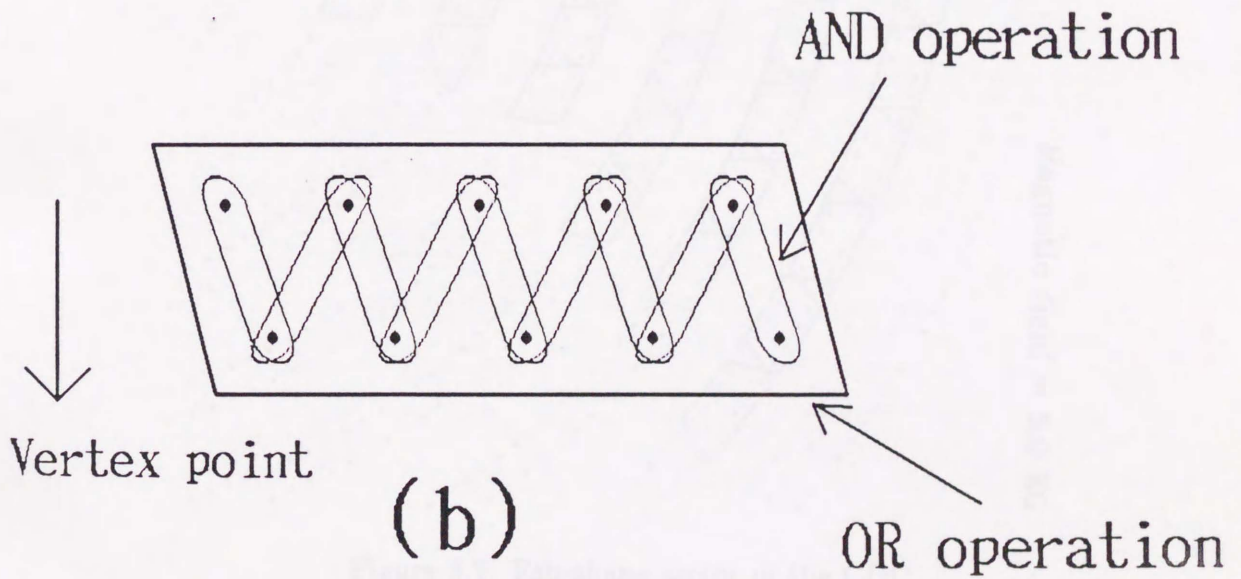
Figure 3.6: Staggered cell structure of the CDC
(a):Staggered cell strucure of CDC. (b):Thick line indicates cell structure for fast track finding in trigger. Thin line shows ANDed operation to avoid hits from X-ray.
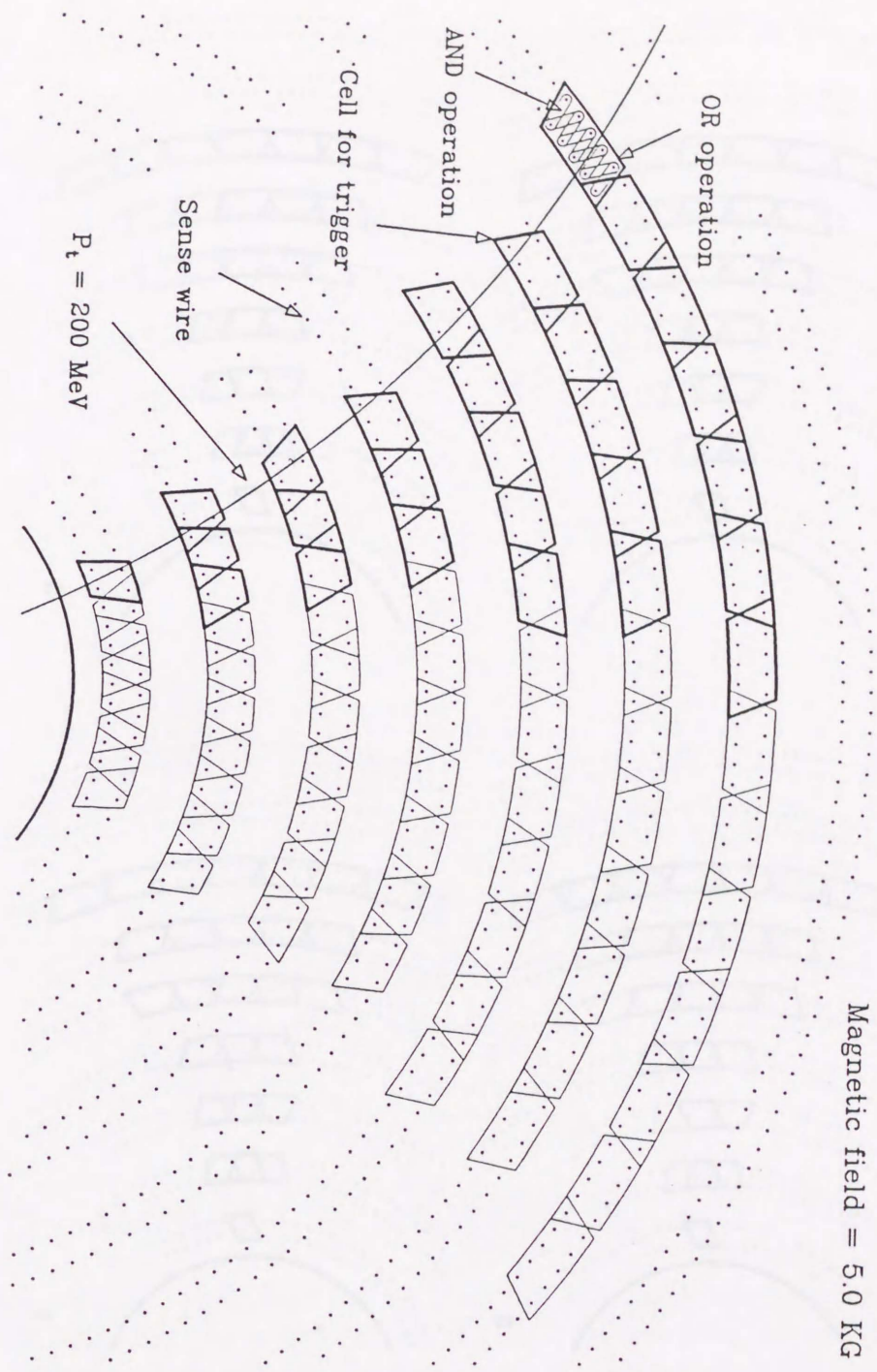
Figure 3.7: Fan-shape sector in the CDC

Signal preparation scheme for TF-CDC. 64 of trigger cell forms 1/8 of whole ϕ coverage.
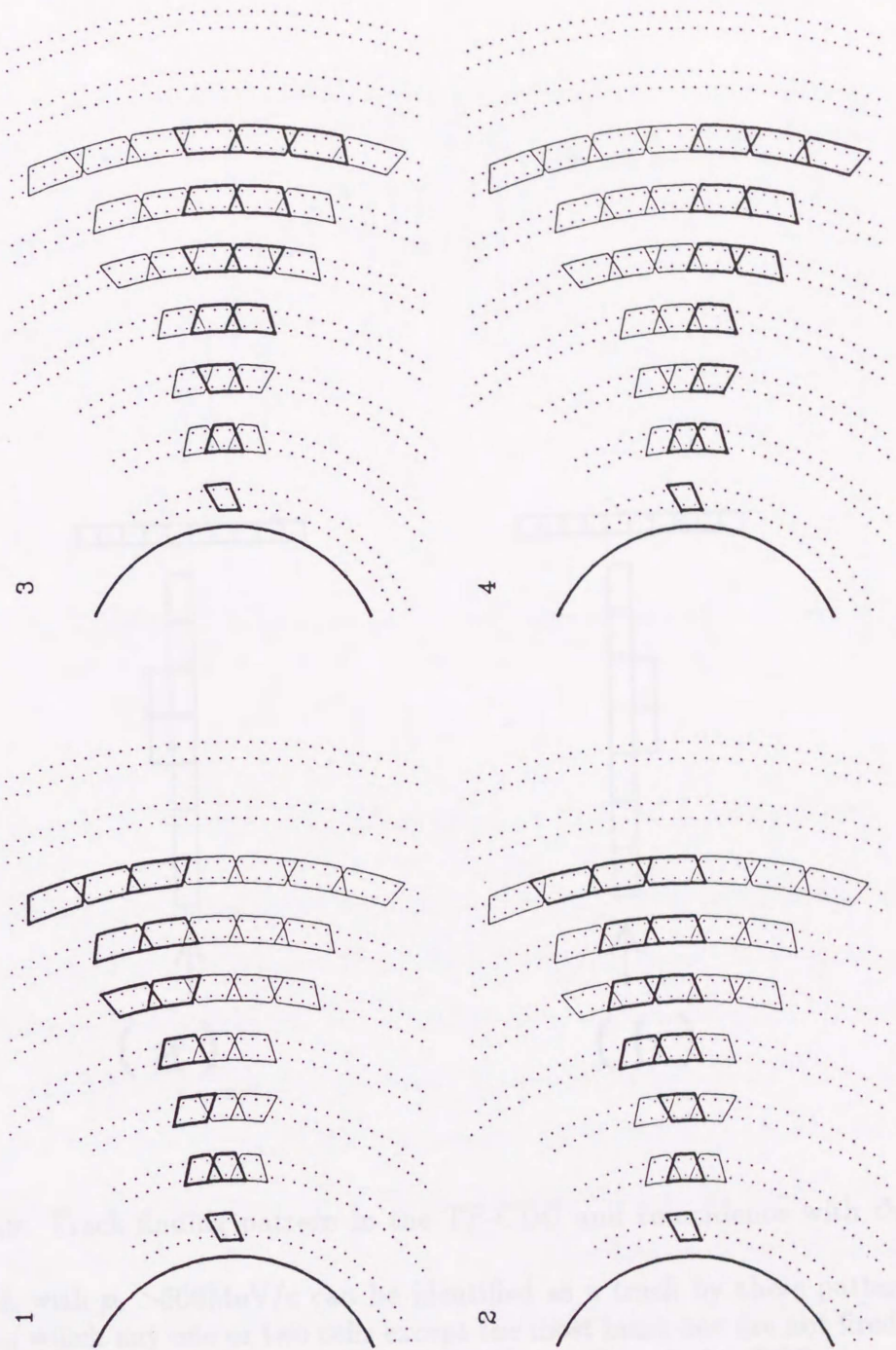
Figure 3.8: Subsectors of fan-shape sector. Each subsector is consited of 12-bit high speed RAM.
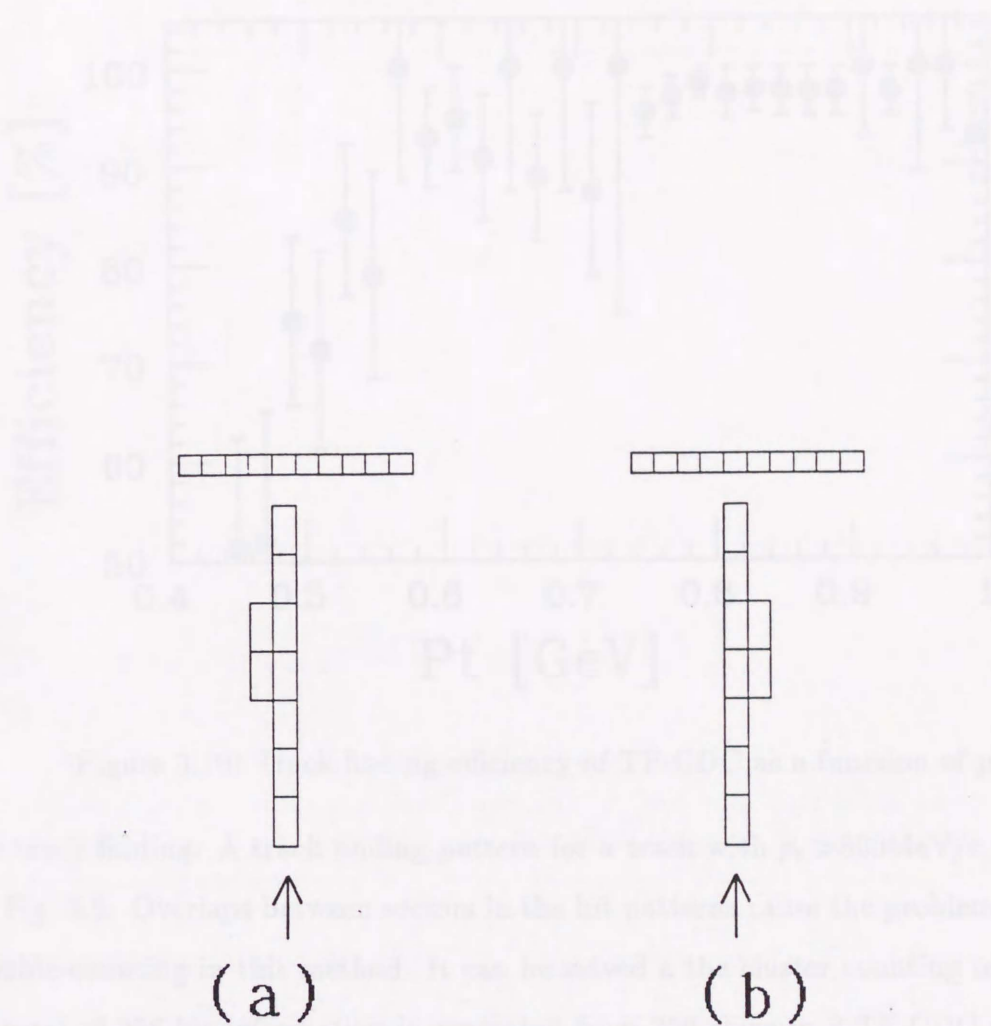
Figure 3.9: Track finding pattern in the TF-CDC and coincidence with the TOF counter.
The track with p_t >500MeV/c can be identified as a track by these pattern. The pattern in which any one or two cells except the most inner one are not fired among the 7 layers should be allowed for track finding. Ten of the TOF counters are coincided with the track flag found by TF-CDC. Arrows indicate the position of track flags in TF-CDC. (a):For left curved track. (b):For right curved track.
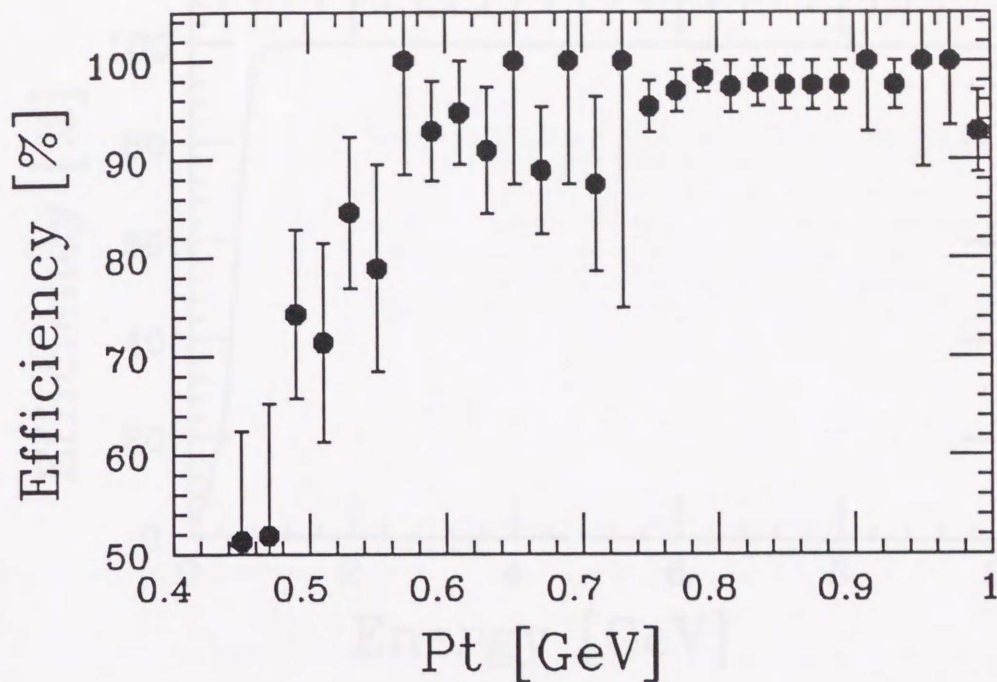
Figure 3.10: Track finding efficiency of TF-CDC as a function of p_t

for track finding. A track finding pattern for a track with $p_t > 500$MeV/c is shown in Fig. 3.9. Overlaps between sectors in the hit patterns cause the problem of track double-counting in this method. It can be solved a the cluster counting technique. A total of 256 bit information is generated from 256 chips in 8 TF-CDC modules, which can be read out via FASTBUS operation and is used for second-level trigger. Four signals which correspond to one basic fan-shape sector are ORed, resulting in 64 track flags which are fed to next-step logic. The efficiency for track finding is shown in Fig. 3.10. For the tracks, it rises at arround p_t=400 MeV/c and reaches to a plateau at p_t=800 MeV/c, with 97.7±0.7%. A detailed description of track finding module for the CDC can be found in the reference[16].

Segment sum trigger of the LG calorimeter

The signals of the 64 track flags from the TF-CDC are sent to the majority logic unit (Lecroy 4532) and multiplicity counting is made there. Then the number of charged tracks is determined. The segment sum trigger of the LG calorimeter requires at least two tracks in the TF-CDC and at least one of the segments of the LG calorimeter
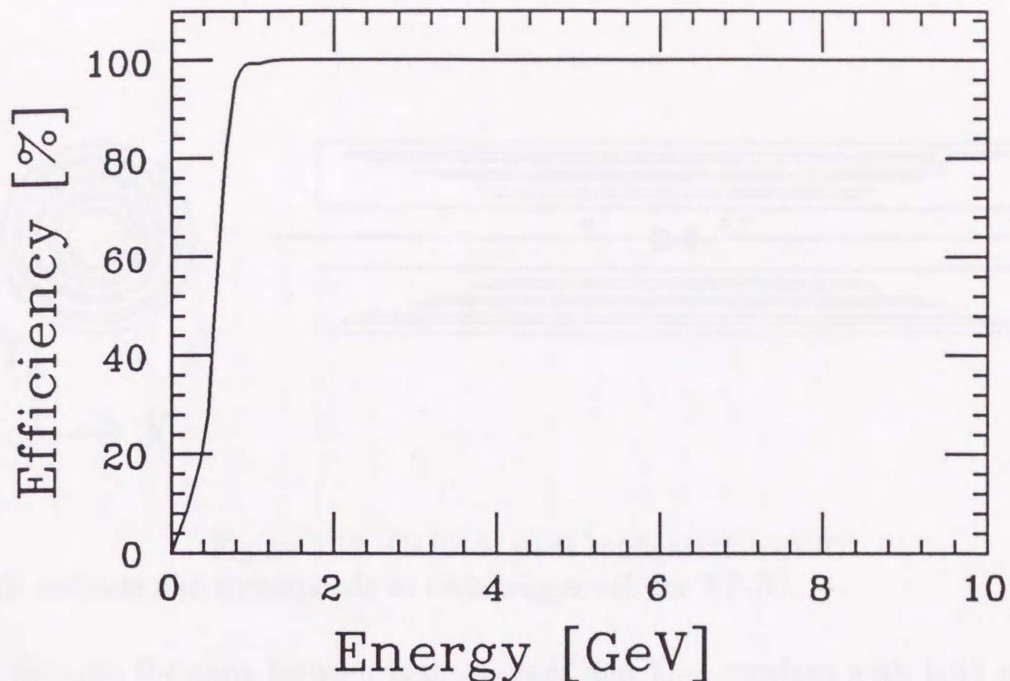
Figure 3.11: Efficiency of the segment sum trigger of the LG calorimeter
The efficiencies are evaluated for the event samples which have only two tracks in the barrel region. This figure indicates the efficiency as a function of deposit energy in the LG calorimeter.

have energy deposits greater than 0.8 GeV. The hit signal of this trigger is sent to the TDM. The efficiency of this segment sum trigger is shown in Fig. 3.11. Fig. 3.11 indicates only the efficiency of the LG calorimeter and does not include the efficiency due to the track finding by TF-CDC. In the region, E≥1.0 GeV the efficiency is more than 99.5%. Then the true efficiency of this segment sum trigger is obtained by multiplied this by the track finding efficiency by the TF-CDC as shown in Fig. 3.10.

Track finding in the IC

The IC of the VENUS is designed as a trigger chamber by making use of hit information of its cathode pads. The configuration of cathode pads is shown in Fig. 3.12. Each cathode pad corresponds to each trigger cell for TF-IC. The trigger cell configuration in 1/8 of the whole ϕ space is shown in Fig. 3.13 when extended in the r-z plane. The particle originated from interaction point passes through their tower in the r-z plane. One 12-bits RAM chip covers adjacent towers for the particles pass-
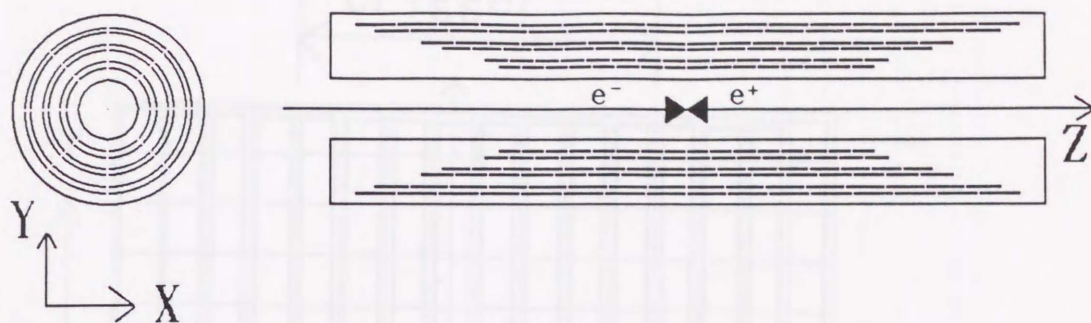
Figure 3.12: Cathode pads configuration of IC
Each cathode pad corresponds to each trigger cell for TF-IC.

ing through the gaps between cathode pads and have overlaps with both of next RAM chips. The hit patterns are generated to make a tower at the box with thick line in Fig. 3.13. On account of the inefficiency of the IC, the hit pattern in which any one cell is not fired in the 6 layers should be allowed in track finding. Such a dead channel is regarded as a hit channel in generating a hit pattern. The IC is used as a z trigger device. However, the TOF counters cover the polar angle region $|\cos\theta| < 0.81$, we use only 8 towers out of 16 towers in the z-direction which cover $|\cos\theta| < 0.86$ in the hit pattern generation.

Total of 128 track flags which consist of 8 components in ϕ times 16 ones in the r-z plane are read out with a FASTBUS operation. Adjacent two signals are ORed, resulting in 64 track flags which are fed to the next-step logic. The track finding efficiency is more than 99.8% and independent of track momentum because on the r-z plane a charged particle runs straight for $p_t \geq 800$ MeV/c. The efficiency is estimated by the events of $e^+e^- \rightarrow e^+e^-$ triggered by the total sum trigger of the LG. The inefficiency is due to that of the IC cell.

Information from the TOF counter

Hits of 96 TOF counters are sent to trigger logics as a set of information for a charged track trigger. Pulses generated by phototubes are discriminated whether
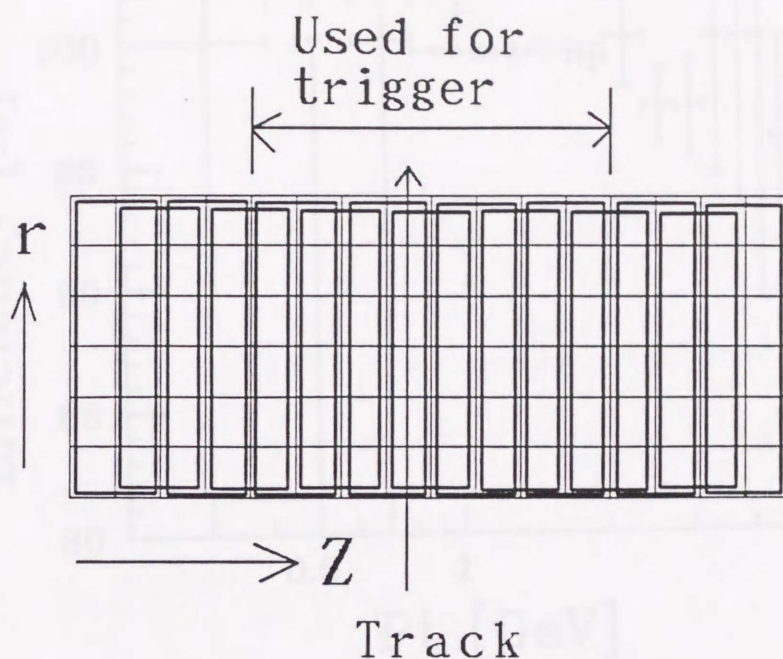
Figure 3.13: Trigger cell configuration of IC pads
Thin line indicates the trigger cell for the TF-IC and the boxes with thick line show the region covered by one 12-bits RAM chip.

they are greater than a given threshold voltage or not, and are converted to a set of the corresponding digital signal. In order to reject an accidental hit caused by thermal noises on phototubes, two digital signals from both sides of a TOF counter are ANDed into one signal. Total 96 of hit information are sent to the next-step logic. The efficiencies are 99.5±0.1, 97.1±0.3 and 96.6±0.4 % for the tracks with 0.8 GeV/c $\leq p_t \leq 2.0$ GeV/c, $p_t > 2.0$ GeV/c, and $p_t > 3.0$ GeV/c, respectively. According to a Monte Carlo study which makes a detailed detector simulation, the efficiency of the TOF counters is on the plateau in the region 0.8 GeV/c $\leq p_t \leq 2.0$ GeV/c and above 2GeV/c it falls gradually with increasing p_t as shown in Fig. 3.14.

Coplanar trigger

The hit information from the TF-IC, TF-CDC and TOF counters are used in the coplanar trigger and the TTL trigger. A hit of the TOF counters is required in association with the hit of the TF-CDC as shown in Fig. 3.9. This coincidence

38
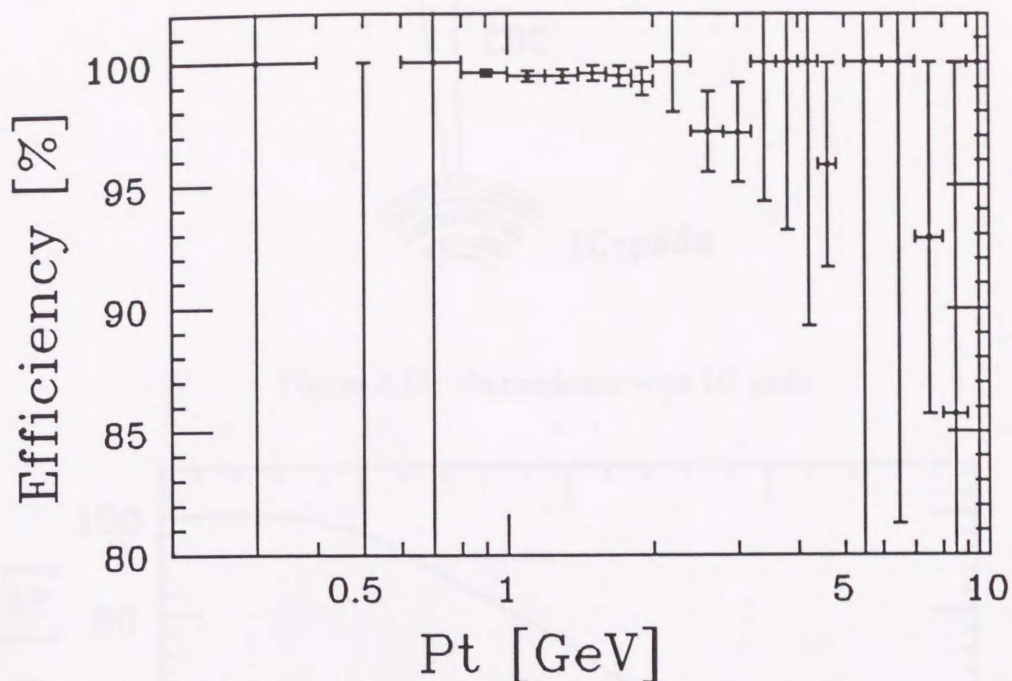
Figure 3.14: The efficiency of the TOF counters as a function of p_t

is effective to reject the cosmic-ray backgrounds in on the on-line stage, because the width of the gate signal for the TOF counters is set smaller than that of other tracking devices. However the coincidence with the TOF counters has a disadvantage to limit the coverage of the transverse momentum $p_t > 800$ MeV/c, since a low-p_t particle can not reach the TOF counters due to Lorentz force from the magnetic field. The results of this coincidence is required an associated hit in TF-IC as shown in Fig. 3.15 to reduce the charged particles in the r-z plane. A sector from the TF-CDC and TOF counters put together with the TF-IC hit covers 90° in ϕ. The 64 sector signals made of the TF-IC, TF-CDC and TOF counters are sent to next step of the TTL trigger and uesd to decide the coplanar trigger by measuring acoplanarity of track pairs. The efficiency of finding single track hit is 96.9 ± 1.0 and 94.6 ± 1.0 % for tracks with 0.8 GeV/c $\leq p_t \leq 2.0$ GeV/c and $p_t > 2.0$ GeV/c, respectively. It is expressed by a product of the efficiencies of the TF-IC, the TF-CDC and the TOF counters. At least one sector hit, which exists in five sectors of opposite side of the referred sector hit, is required by the coplanar trigger in order to pick up the back-to-back event. Fig. 3.16 shows the efficiency as a function of
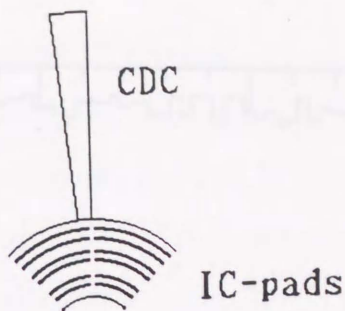
Figure 3.15: Coincedence with IC pads
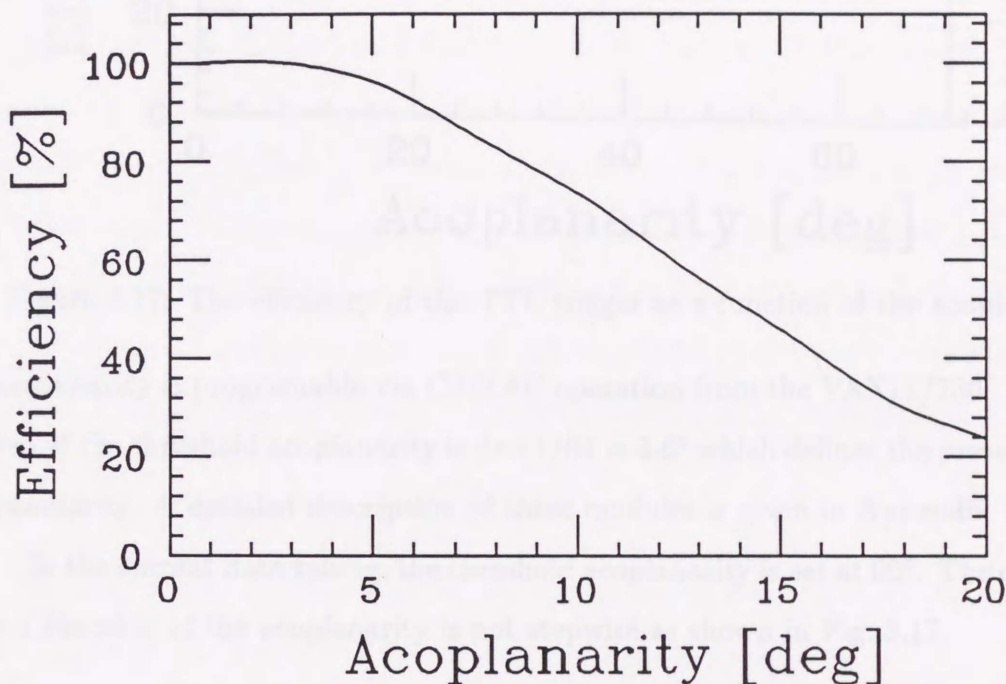
Figure 3.16: The efficiency of coplanar trigger for low momentum track as a function of the acoplanarity, when triggered by the TTL trigger

acoplanarity ($\Delta\phi$) evaluated for the two track data samples which are triggered by the TTL trigger. The region with $\Delta\phi \leq 3°$ and $\Delta\phi \leq 10°$ is enough efficient for low-mometum ($p_t \leq 2\text{GeV/c}$) and high-momentum tracks, respectively.

Two-track limited trigger

The TTL trigger is made to have more acceptance for acoplanar events such as $e^+e^- \rightarrow \mu^+\mu^- + X$. The existence of a pair of tracks for which acoplanarity is smaller than a given threshold is required. Specific look-up table modules on CAMAC are designed and employed for this purpose. The look-up table to give the threshold
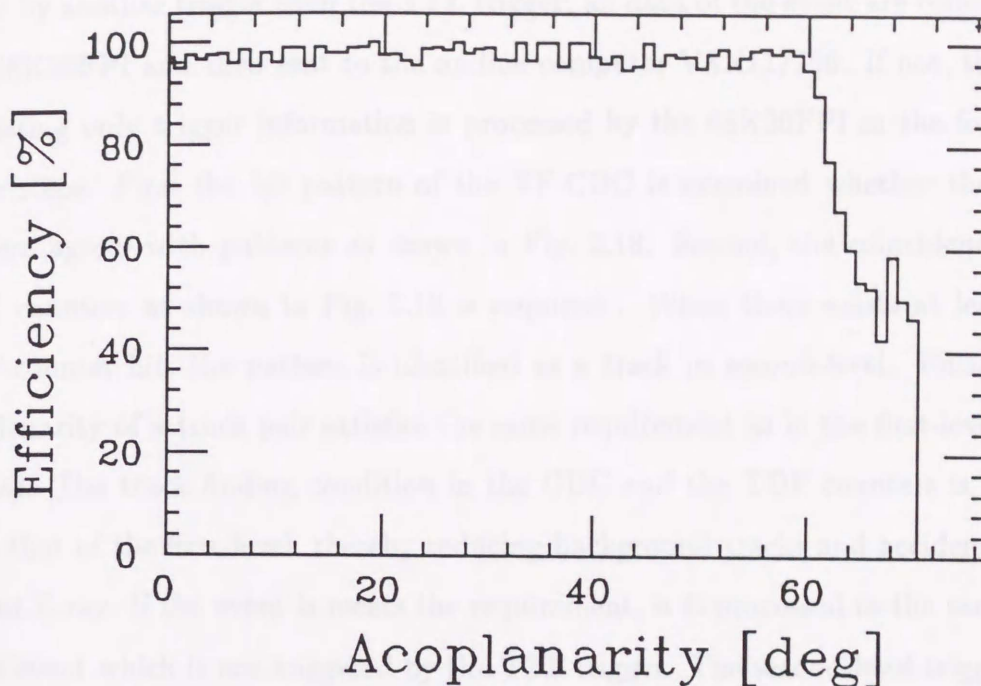
Figure 3.17: The efficiency of the TTL trigger as a function of the acoplanarity acoplanarity is programable via CAMAC operation from the VAX11/780. The unit step of the threshold acoplanarity is $2\pi \times 1/64 = 5.6°$ which defines the present sector granularity. A detailed description of these modules is given in Appendix B.

In the current data taking, the threshold acoplanarity is set at 60°. The efficiency as a function of the acoplanarity is not stepwise as shown in Fig. 3.17.

3.2   Second-level trigger

The number of TTL-triggered events amounts to about half of the whole first-level triggered events and the data size of a TTL triggered event is larger than an averaged data size of the whole triggered events, since the TTL trigger requires the existence of some tracks in the CDC. Filtering the TTL-triggered events by second level trigger is effective to reduce the data size and the event number to be stored in the magnetic tape library. First, only trigger information of a first-level triggered event is collected by a 68K20FPI microprocessor module on FASTBUS. The trigger information consists of hit information in TDM, TF-IC, TF-CDC, TOF-counter, and so on, and it is a small part of the whole data. Second, if the event is trig-

41

gered by another trigger than the TTL trigger, all data of the event are collected by the 68K20FPI and then sent to the on-line computer VAX11/780. If not, the data consisting only trigger information is processed by the 68K20FPI in the following three steps: First the hit pattern of the TF-CDC is examined whether the input pattern agrees with patterns as shown in Fig. 3.18. Second, the coincidence with TOF counters as shown in Fig. 3.18 is required . When there exists at least one TOF-counter hit, the pattern is identified as a track in second-level. Finally, the acoplanarity of a track pair satisfies the same requirement as in the first-level TTL trigger. The track finding condition in the CDC and the TOF counters is severer than that of the first-level, thereby reducing background tracks and accidental hits due to X-ray. If the event is meets the requirement, it is processed in the same way as an event which is not triggered by the TTL trigger. The second-level trigger system has employed from the run in June 1989 and succeeds in reducing the number of the TTL triggerd events by about 50%. The inefficiency of the second-level trigger due to the hit pattern constraints is negligibly small. This is comfirmed by Monte Carlo studies.

The trigger system of the VENUS has operated with good stability and reliabilty. The trigger rate is typically 5 Hz under a good beam condition.
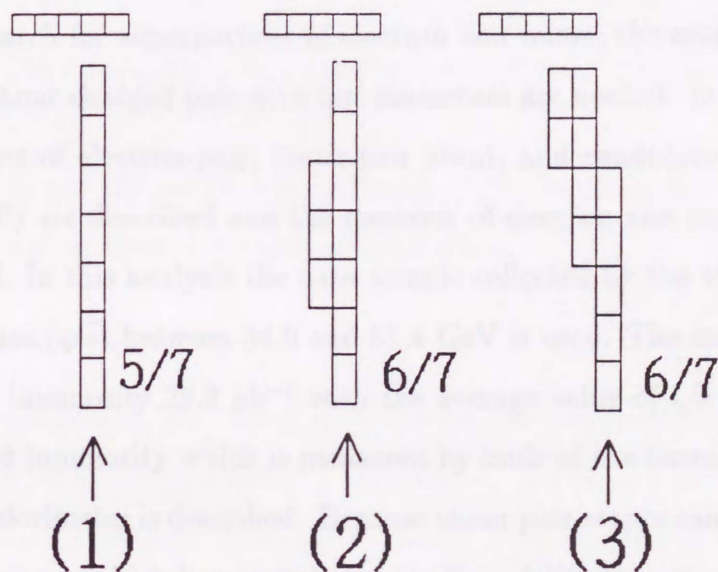
Figure 3.18: TF-CDC hit pattern and TOF coincidence searched by the second-level trigger
(1):required layer hit 5 out of 7. (2) and (3):required layer hit 6 out of 7. The patterns show for only Fig. 3.9-(a) case in the first-level trigger. For Fig. 3.9-(b) case all of pattern in this figure should be reversed.

Chapter 4

Data Analysis

In order to search for superpartner of electron and muon, the event samples which have an acolpanar charged pair with low mometum are needed. In this chapter, the event selections of electron-pair, muon-pair event, and candidate for heavy stable particles (HSP) are described and the methods of electron and muon identification are disscused. In this analysis the data sample collected by the VENUS at center-of-mass energies ($\sqrt{s}$) between 54.0 and 61.4 GeV is used. The data correspond to an integrated luminosity 29.2 pb^{-1} with the average value of $\sqrt{s}$ being 58.5 GeV. The integrated luminosity which is measured by both of the barrel calorimeter and the end-cap calorimeter is described. Because muon-pair events can be detected only by the TTL trigger which has operated since Nov. 1988, the integrated luminosity for the muon-pair events is 17.7 pb^{-1} taken at $\sqrt{s}$ between 54.0 and 61.4 GeV with the average value being 60.0 GeV. The integrated luminosity at each center-of-mass energy is shown in Table 4.1.

4.1 Pre-selection

Collected data samples contained various background events which are not orginated from e$^+$e$^-$ collisions such as those due to beam-beampipe, beam-gas interactions, and cosmic-ray. In order to reject these background events, the pre-selection called "Process 1" is applied to all data samples. The data samples passed through "Process 1" are further processed by "Low-mul process 2" to get low-multiplicity charged-track events. The above two selections are generally adopted in VENUS analysis proce-

44

$\sqrt{s}$	$\int L dt$	data	$\sqrt{s}$	$\int L dt$	data	$\sqrt{s}$	$\int L dt$	data
54.0	855	e,μ	57.5	124	e,μ	59.125	84	e,μ
55.0	1756	e	57.75	95	e,μ	59.25	78	e,μ
56.0	5254	e	58.0	256	e,μ	59.5	92	e,μ
56.5	858	e	58.5	1122	e,μ	60.0	3413	e,μ
57.0	3699	e	59.0	1450	e,μ	60.8	4413	e,μ
57.25	76.1	e,μ	59.05	489	e,μ	61.4	5115	e,μ

Table 4.1: Summary of the integraded luminosity

The energy $\sqrt{s}$ and the luminosity are in units of GeV and nb^{-1}, respectively. The letters e and μ in the column of 'data' indicate that data used in the analysis of electron-pair and muon-pair event selection, respectively. For heavy stable particle the same data as electron-pair are used.

dure. Finally to get the events which contain only two chraged-tracks, "Two-track selection" is applied prior to particle identification.

4.1.1 Process 1

The selection criteria of "Process 1" is based on the energy deposit in calorimeters and/or charged-track reconstruction in the CDC. The energy calibration and clustering of shower energy deposits are performed for the barrel and end-cap calorimeters. The charged track reconstruction in the CDC is also carried out. Both of the abbove event reconstructions are applied to all triggered events. The track reconstruction efficiencies are larger than 89% for charged particles in the polar angle range $| \cos \theta | < 0.9$, when the track is isolated from other charged tracks [27], while that for charged particles with $| \cos \theta | < 0.75$ is 99.5±0.1%, which is deduced from a study of Bhabha events[31]. Requirements of "Process 1" confirm the constraints of the event trigger. If at least one of the following requirements is satisfied, the event is accepted as an input for "Process 2".

1. Total shower energy deposited in the barrel calorimeter is larger than 3.0 GeV for the event accepted by the total energy trigger of the LG calorimeter.

2. Total shower energy deposited in the end-cap calorimeter is larger than 3.0 GeV for the event accepted by the total energy trigger of the LA calorimeter.

45

3. Total shower energy deposited in the end-cap calorimeter is larger than 1.5 GeV for the event accepted by the sector sum energy trigger of the LA calorimeter.

4. At least two "tracks" are detected in the CDC for the event accepted by the coplanar trigger or the TTL trigger.

5. At least one "track" is detected in the CDC and the total energy of the barrel calorimeter is larger than 0.5 GeV for the event accepted by the segment sum trigger of the LG calorimeter.

Here, the reconstructed "track" is defined as follows:

- The track is three-dimensionally reconstructed where $N_{axial} \geq 10$ and $N_{slant} \geq 4$, where N_{axial} and N_{slant} are the number of hit for axial wire and slant wire, respectively.

- The radial distance of the closest approach of the track to the interaction point in the r-ϕ plane, R_{min}, and z-cordinate of this point, Z_{min}, meet the conditions $| R_{min} |< 7$cm and $| Z_{min} |< 30$cm, respectively. The R_{min} is defined to be positive if the origin is inside the circle of reconstructed track.

- The transverse momentum to the beam axis, p_t, should be $p_t \geq 0.2$GeV/c.

The reduction ratio due to "Process 1" depends on the beam condition. About 40% of all triggered events survive for "Process 2" on the average.

4.1.2 Low-mul process 2

The "Low-mul process 2" selection is applied to the data samples passed through the "Process 1", in order to select charged-track event using only the infromation from the CDC. The selection condition is severer than that of "Process 1" in respect to charged-track reconstruction, since the reconstruction quality of low-multiplicity event is better than that of high-multiplicity one. The events are accepted when they satify the following requirements:

1. The number of reconstructed tracks is greater than 1 and less than 21. The reconstructed tracks may contain those tracks which are not thress-dimensionally reconstructable.

2. The Number of "good track" is greater than 1. The "good track" satisfies the followings:

   - $N_{axial} \geq 10$ and $N_{slant} \geq 4$,

   - $|R_{min}| < 2cm$ and $|Z_{min}| < 15cm$ to reject the cosmic-ray events.

3. At least a track that satifies the requirement 2 meets the the condition: $Q/p_t \leq 0.5(GeV/c)^{-1}$, where Q is charge. This condition requires that the track has whether the positive charge and high transverse momentum ($p_t \geq 2GeV/c$) or the negative charge in order to reject beam-pipe events in which protons are most likely to appear.

4.1.3 Two-track event selection

Two-track event selection is performed to reject multitrack events. The number of "good track" is 2 only with no "other track". The "good track" in this selection satisfies the followings:

- $N_{axial} \geq 10$ and $N_{slant} \geq 4$,

- $|R_{min}| < 2cm$ and $|Z_{min}| < 6cm$,

- $|\cos\theta| < 0.75$,

- $p_t \geq 400MeV/c$.

The polar angle limit, $|\cos\theta| = 0.75$, correponds to the position which is inner by two modules of LG measured from the end of the barrel calorimeter. "Other track" requires the following conditions:

- $N_{axial} \geq 10$ and $N_{slant} \geq 4$,

- $|R_{min}| < 2cm$ and $|Z_{min}| < 6cm$,

47

- $|\cos\theta| < 0.85$,

- $p_t \geq 200\text{MeV/c}$.

The polar angle limit, $|\cos\theta| = 0.85$, correponds to the position which is inner by two modules of LA measured from the outer end of the end-cap calorimeter.

After this three-step preselection, the data samples are processed by particle identification procedures for electron, muon and heavy stable particle.

4.2   Electron-pair event selection

Electron-pair event sample is selected by the track momentum determined with the CDC and the energy deposit in the LG calorimeter. The opening angle of electron-pair is required to be greater than $10°$, in order to reject the process $\gamma \rightarrow e^+e^-$. An electron track is identified by the following requirements:

1. The polar angle of track must satisfy the condition $|\cos\theta| < 0.75$ which corresponds to the coverage of the barrel calorimeter.

2. Shower energy deposit in the barrel calorimeter, associated withe the track is greater than 1 GeV.

3. The condition $0.5 \leq E/P \leq 1.5$ must be satisfied, where E is the shower energy deposit associated with the track whose monetum is P.

The electron identification efficiency is dominated by a cut in the E/P distribution whose example is shown in Fig. 4.1 for $E \geq 1$ GeV and $|\cos\theta| < 0.75$. The inefficiency in this identification is due to the momentum and the shower energy resolutions. It may be evaluated by a formula: inefficicency $= \frac{N_{0 \leq E/P < 0.5} + N_{1.5 < E/P \leq 2}}{N_{0 \leq E/P \leq 2}}$, where $N_{0 \leq E/P < 0.5}$, $N_{1.5 < E/P \leq 2}$, and $N_{0 \leq E/P \leq 2}$ are the number of tracks which satisfy $0 \leq E/P < 0.5$, $1.5 < E/P \leq 2$, and $0 \leq E/P \leq 2$, respectively. It is found to be $1.8\pm0.2\%$ for tracks which are associated with the shower energy of greater than 1 GeV, while for those with $E> 2$ GeV, the inefficiency becomes $2.1\pm0.3\%$. The
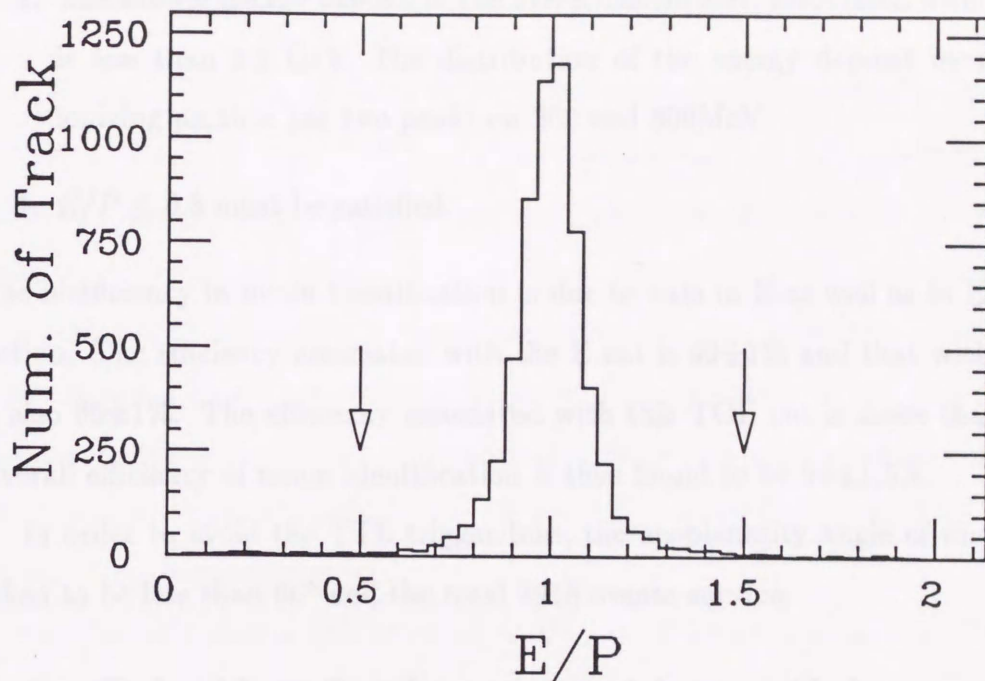
Figure 4.1: E/P distribution

Tracks distributed in this histogram are selected from the electron-pair event sample before apllying the E/P cut. The cut points are indicated by arrows. σ of this distribution is 0.074.

inefficicency due to bremsstrahlung and hard-photon emmission is estimated to be $1.5\pm1\%$ and $1.9\pm1\%$, respectively.

4.3 Muon-pair event selection

The selection for muon-pair events is performed by using the track momentum, the energy deposit in the LG calorimeter, and the time-of-flight of particle. We select those events in which only two tracks are identified as muon in the barrel region, $|\cos\theta| < 0.75$. Then the muon identification is described as follows:

1. The transeverse momentum is greater than 800 MeV/c. This is required by the TTL trigger condition.

2. Difference in time-of-flight for two tracks is less than 5 nsec. For cosmic-ray events the difference is typically 10 ns.

49

3. The shower energy deposit in the barrel calorimeter, associated with the track, is less than 1.5 GeV. The distribution of the energy deposit by minimum-ionizing particle has two peaks on 200 and 600MeV.

4. $E/P \leq 0.8$ must be satisfied.

The inefficiency in muon identification is due to cuts in E as well as in E/P distribution. The efficiency associated with the E cut is 99±1% and that with E/P cut is also 99±1%. The efficiency associated with this TOF cut is more than 99.7 %. Overall efficiency of muon identification is thus found to be 98±1.5%.

In order to avoid the TTL trigger bias, the acoplanarity angle of muon-pair is taken to be less than 60° and the total 3918 events survive.

4.4   Selection for heavy stable particles

Charged and heavy stable particle is identified with its velocity determined from the track path length and the time-of-flight. If a heavy stable particle pair is produced, it appears like muon-pair production due to single photon exchnage. At first, back-to-back charged pair events are selected with the opnening angle of the pair being greater than 170°. The polar angle, θ of both tracks must satisfy $|\cos\theta| < 0.65$ to avoid the massive region of our detector. The transverse momentum of both tracks is selected to be greater than 800 MeV/c to avoid the TTL trigger bias. Next, the difference in time-of-flights of the tracks is chosen to be within 5ns to reject cosmic-ray events. Finally, in order to guarantee the quality of time-of-flight measurement, the hit positions for both tracks measured with the TOF counters are within 12cm from the position which is determined by extrapolating the CDC-tracks and photo-tubes at the both end of these TOF counters must be fired. Since the spatial resolution of TOF counter in the z-direction is 4cm, the efficiency due to this hit position cut is estimated to be more than 99.5%. The efficicncy that the the both photo-tubes fire is more than 99.0% in the event sample obtained by the TTL trigger. The overall selection efficiency for charged heavy stable particle pair production is estimated to be 97% and the total 991 events survive.

4.5   Luminosity measurement

For the normalization of data, three indepndent measurements for the luminosity are available at the VENUS. These measurement are performed by detecting Bhabha events with the LG, LA, and LM. The measurement with the LM suffers from large beam backgrounds such as spent electrons and hence results in a large systematic error amounting approximately to 10%. The measurement with the LA has a systematic error of about 4% due to the uncertainty in the cluster position and backgrounds from $e^+e^- \rightarrow \gamma\gamma$ events because of a poor tracking capability in the forward region. We accordingly use the information from the LG and CDC for the luminosity measurement.

The events satisfied the following requirements are selected as the Bhabha candidates in the barrel region [31]:

1. The number of reconstructed tracks (defined in 4.1.1) with $p_t > 1$ GeV/c in the CDC is from two to four.

2. At least there exists one back-to-back pair (the acollinearity angle less than 10°).

3. Both tracks of this collinear pair satisfy $| \cos\theta | \leq 0.743$.

4. Each track of the pair is associated with a shower cluster in the barell calorimeter within a cone of 10° around the track, and the energy of the cluster is larger than 1/3 of the beam energy.

The backgrounds from multihadronic events, τ-pair production, and double conversion of $\gamma\gamma$ events are estimated to be 0.1%, 0.3%, and 0.1%, respectively. The corrections due to the dead lead-glass modules (0.7%), failure of the track reconstruction (0.4%), and event loss by the bremsstrahlung in the detector are taken into account. The correction amounted to 2.4% in total. The trigger inefficiency is estimated to be less than 0.1%. The acceptance is evaluated by a Monte Carlo simulation which includs the contribution from all of the diagrams of electroweak

interactions up to the order α^3 [32]. The contamination from radiative events is estimated to be 1.5%. The major source of systematic error is the uncertainty in the detector acceptance. It is estimated by changing the cut value for the polar angle of the charged tracks and the acollinearity angle between tracks. The systematic error in the luminosity measurement is estimated to be 2.7% in total.

Chapter 5

Results and Discussion

We discuss in this chapter physical implications of the obtained data. First we discuss two photon processes, $e^+e^- \to e^+e^-e^+e^-$ and $e^+e^- \to e^+e^-\mu^+\mu^-$, and their backgrounds in the first two sections. Next, we give a detailed discussion on search for superpartner of electron and muon.

5.1 Background for two-photon process

In this section we examine the background processes for two-photon process. The backgrounds into the lepton production events from two-photon collisions have two different origins. One is the events coming from real e^+e^- collision, while the other from collisions between electron or positron beam and beam pipe materials or gas in the vacuum chamber. The former comes from the processes, $e^+e^- \to \tau^+\tau^-(\gamma)$, $e^+e^- \to \mu^+\mu^-(\gamma)$, $e^+e^- \to e^+e^-\tau^+\tau^-$, and $e^+e^- \to e^+e^- + \text{hadrons}$, while the later results from beam-gas and beam-pipe events.

5.1.1 Backgrounds from e^+e^- collision

The lepton production in the electroweak processes $e^+e^- \to e^+e^-(\gamma)$, $e^+e^- \to \mu^+\mu^-(\gamma)$, $e^+e^- \to \tau^+\tau^-(\gamma)$ [34], and $e^+e^- \to e^+e^-\tau^+\tau^-$ [35] have a dominant contribution in the present experiment and their cross sections are theoretically well known. These are evaluated by a Monte Carlo simulation which takes a detailed account of our detector performances. The contamination from hadron production will be discussed separately.
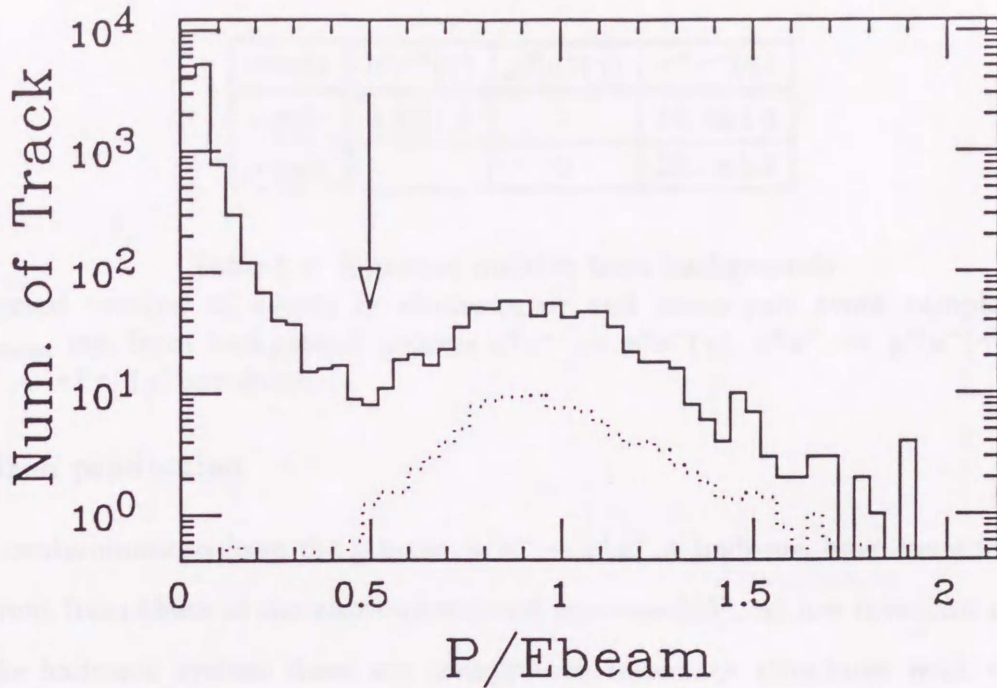
Figure 5.1: P/E$_{beam}$ distribution

The solid line shows the distribution of P/E$_{beam}$ for muon-pair events sample, while that for $e^+e^- \rightarrow \mu^+\mu^-(\gamma)$ is indicated by the doted line. The arrow shows a cut point.

Lepton production

A pair of electron or muon from single photon and/or Z^0 exchange has a momentum equal to the beam energy. Fig. 5.1 shows the P/E$_{beam}$ distribution for muon-pair event sample, where E$_{beam}$ is the beam energy. We rejecte the events which have at least the track with P/E$_{beam} \geq 0.5$, as coming from single-photon exchange event. The number of expected events by a Monte Carlo study from $e^+e^- \rightarrow e^+e^-(\gamma)$, $e^+e^- \rightarrow \mu^+\mu^-(\gamma)$, and $e^+e^- \rightarrow \tau^+\tau^-(\gamma)$ in electron-pair and muon-pair event sample after this cut are shown in Table 5.1. However, the events $e^+e^- \rightarrow e^+e^-\tau^+\tau^-$, where τ decays further into electron or muon, escape from the above cut, and this background contamination should be subtracted. The number of expected events for this background is estimated to be 8±2 and 5±1 for electron-pair and muon-pair events, respectively, from the Monte Carlo studies.

events	$e^+e^-(\gamma)$	$\mu^+\mu^-(\gamma)$	$\tau^+\tau^-(\gamma)$
e-pair	4.2 ± 1.9	-	18.8 ± 1.4
μ-pair	-	0	28.1 ± 1.3

Table 5.1: Expected number from backgrounds

Expected number of events in electron-pair and muon-pair event sample after P/E_{beam} cut from background process $e^+e^- \rightarrow e^+e^-(\gamma)$, $e^+e^- \rightarrow \mu^+\mu^-(\gamma)$, and $e^+e^- \rightarrow \tau^+\tau^-(\gamma)$ are shown.

Hadron production

The contaminations from the process, $e^+e^- \rightarrow e^+e^- +$ hadrons, have some features different from those of the above-mentioned processes[36]. At low invariant masses of the hadronic system there are complicated resonance structures with various peak values and widths, whereas at high invariant masses the cross section is well determined by the quark-parton model (QPM)[37]. We must treat the region above $W\approx 2.0\text{GeV}$, and here give up to estimate the hadron backgrounds using only by the resonance structure or by QPM. Instead, we estimate the hadronic background by studying the detector response for charged pion.

The hadronic response of the LG calorimeter is studied in a beam test (see Apendix C). Distribution of the shower energy deposit in the LG calorimeter by charged pion is almost the same as that of the minimum ionizing particle. However, pion gives a long tail in the high energy side where E/P is greater than 1 due to the reactions $\pi^-+p\rightarrow \pi^0+n$ and $\pi^++n\rightarrow \pi^0+p$. In the two-track event sample, the event in which one track is identified as that due to the minimum ionizing particle and the other has a large shower energy deposit in the LG, is regarded as either of hadron-pair production resulting from two photon collision or electron-muon pair from $e^+e^- \rightarrow e^+e^-\tau^+\tau^-$. The selection criteria for the minimum ionizing particle is E< 1.0 GeV and E/P < 0.5. The requirement for electron track is $E > 1.0$ GeV. The histogram in Fig. 5.2 shows the E/P dstribution for the electron tracks, whereas the solid curve is a gaussian distribution fitted to the data around the peak at E/P = 1. LIt corresponds to electron-muon events and the number of events estimated
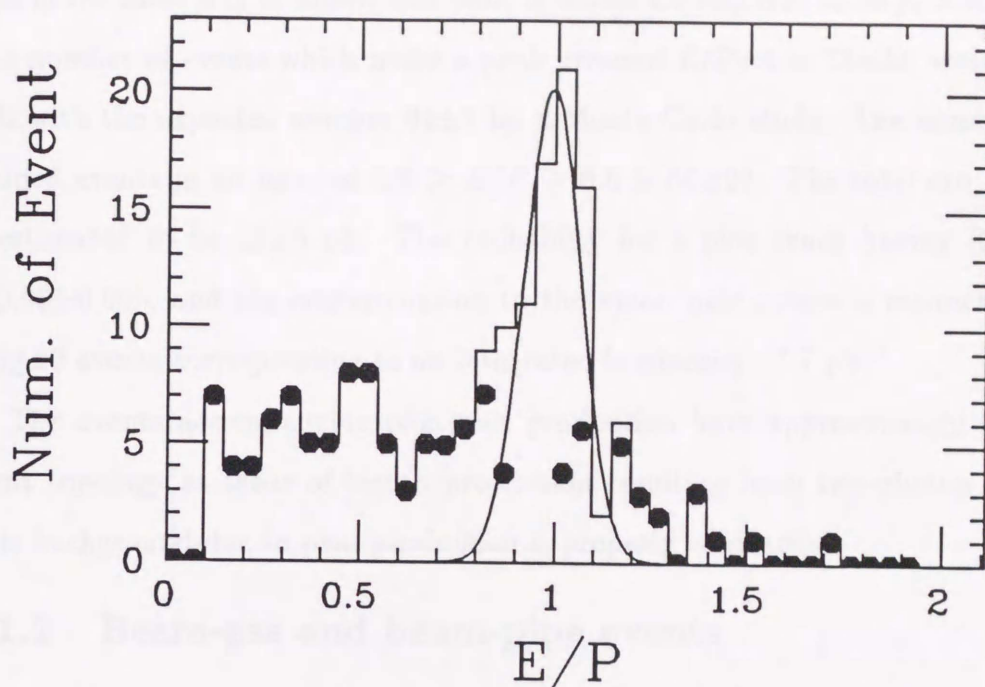
Figure 5.2: E/P distribution of the tracks with E>1GeV

E/P distribution of electron candidate tracks with E>1 GeV is indicated. The data sample is selected from two-track events (see in 4.1.3) by requiring one to be a minimum ionizing one and the other to be with E>1GeV. The solid curve indicates a gaussian distribution fitted to the data around the peak at E/P = 1 with σ being 0.94. The plot shows the difference between the data and the gaussian fit.

from the fit is 78±30, while that for $e^+e^- \rightarrow e^+e^-\tau^+\tau^-$ is estimated to be 69±8 by means of Monte Carlo studies. These values are in good agreement with each other. The plot in Fig. 5.2 indicates the difference between the data and the fit. The number of remained events in an interval $1.5 \geq E/P \geq 0.5$ is 64±30 corresponding to an integrated luminosity 19.2 pb^{-1}. According to the results of beam test, the probability for a track having E/P$\geq$ 0.5 is 10±1% and then the probabilty for only one track of pion-pair having E/P$\geq$ 0.5 is estimated to be 20±2 %. The total cross section of charged pion pair events with an acceptance cut which is the same as electron-pair event selection is estimated to be 17±9 pb. The probability for both of pion tracks having the E/P value greater than 0.5 is 1 %. The backgrounds from pion pair events is thus estimated to be 5±3 events corresponding to an integrated luminosity 29 pb^{-1}.

For muon-pair events sample, the contamination from pion pair events is evalu-

56

ated in the same way as above, but both of tracks are required to be $p_t > 0.8 \text{GeV/c}$. The number of events which make a peak arround E/P=1 is 73±20, which agrees well with the expected number 94±7 by a Monte Carlo study. The number of remained events in an interval $1.5 \geq E/P \geq 0.5$ is 60±20. The total cro s eection is estimated to be 15±5 pb. The probabilty for a pion track having E/P≥ 0.8 is 0.98±0.005, and the contamination to the muon pair events is estimated to be 265±90 events corresponding to an integrated luminosity 17.7 pb^{-1}.

The events accompanying pion pair production have approximately the same event topology as those of lepton production resulting from two-photon collision. This background due to pion production is properly subtracted.

5.1.2   Beam-gas and beam-pipe events

The events due to beam-gas and beam-pipe interactions may have the same topological features as those due to two-photon collisions. Both of them have a few low momentum tracks and are well balanced in transverse momentum. The contamination of beam backgrounds can be estimated by examining the distribution of Z_{min} described in subsection 4.1.1. For the data sample selected by 'Low-mul Process 2' in subsection 4.1.2, the distribution of the average value of Z_{min} taken for a track pair is shown in Fig.5.3, where the histogram shows the data while the curve is a gaussian fit. The fit is in good agreement with the data and if the events in the region where $| Z_{min} |$ is greater than 5 cm are regarded as beam backgrounds, the Z_{min} distribution of these backgrounds becomes flat, in conformity with the fact that they occur homogeneously along the beam pipe. The contamination due to these backgrounds is estimated to be less than 0.1% for electron-pair event and to be 0.4% for muon pair event sample. Most of the tracks in the beam backgrounds are likely to be hadrons such as charged pions and protons and they do not deposit much energy in the LG calorimeter as electron does. As a result, misidentification of these backgrounds as an electron-pair event is less than as a muon-pair event.

If beam-gas, beam-pipe, or cosmic-ray event occurs concurrently with the real two-photn collision, the event has tracks more than three and is rejected by the
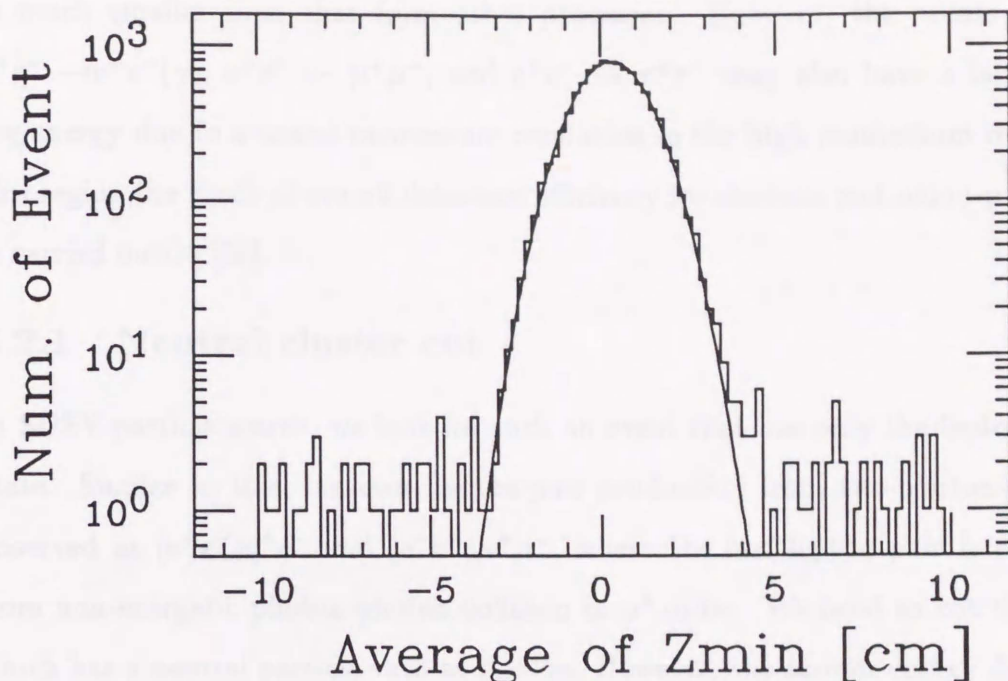
Figure 5.3: Average of Z_{min}

The histogram indicates the average value of Z_{min} taken for a track pair in 'Low-mul Process 2' data sample and the solid curve shows a gaussian fit.

two-track event selection in subsection 4.1.3. The inefficiency due to this possibility is estimated by studying Bhabha events sample. The events are selected in Bhabha events sample with both of the following requirements; large energy deposit in the barrel calorimeter and the existence of additional tracks isolated from the high energy electron tracks. The 3361 of Bhabha events are investigated but none of the event with additional tracks is found and here the inefficiency is estimated to be less than 0.1%.

5.2 Lepton production from two-photon collision

The events for lepton production resulting from two-photon collision are the dominant backgrounds for superpartner search, since event topology is supposed to be similar to that of SUSY event. The latter may have a large acoplanarity as well as a large missing energy. Then we should study about two photon lepton production such as $e^+e^- \rightarrow e^+e^-e^+e^-$ and $e^+e^- \rightarrow e^+e^-\mu^+\mu^-$ in order to check overall detection efficiency in low momentum region. The contribuiton from $e^+e^- \rightarrow e^+e^-\tau^+\tau^-$

is much smaller than that from other processes. However, the events such as $e^+e^- \rightarrow e^+e^-(\gamma)$, $e^+e^- \rightarrow \mu^+\mu^-$, and $e^+e^- \rightarrow \tau^+\tau^-$ may also have a large missing energy due to a coarse momentum resolution in the high momentum region. In this region the check of overall detection efficiency for electron and muon-pair event is carried out[39][38].

5.2.1 Neutral cluster cut

In SUSY-particle search, we look for such an event that has only the leptonic final state. Similar to this, however, lepton-pair production from two-photon collision observed as $(e^+e^-)e^+e^-$ and $(e^+e^-)\mu^+\mu^-$, where the last lepton pair is produced from non-energetic photon-photon collision in α^4 order. We need to cut the event which has a neutral particle such as photon. However, the shower energy deposited in the barrel and the end-cap calorimeter should been treated separately, since these devices have different performances compared with the LG and LA calorimeters.

In the barrel region there is only lepton track-pair in our event sample. Shower clusters which are not associated to a lepton track can be identified as neutral cluster. Fig. 5.4 shows the opening angle distribution of neutral showers measured with the LG calorimeter, where the opening angle is defined between the nearest lepton track. We observe a peak around 5° and a flat distribution above 15°. The neutral clusters within opening angle$\leq$ 15° seem to associate with a lepton track and are not cared in two-photon analysis. The cluster energy distibution for the events with their opening angle being greater than 15° is shown in Fig. 5.5. We cut the events which have at least one neutral cluster, E$\geq$1 GeV with their opening angle $\geq$ 15°.

Fig. 5.6 shows an example of distribution of the shower energy in the end-cap calorimeter for lepton-pair events. The shower clusters with their energy being less than 1 GeV are neglected in this selection. In experimental studies of two-photon interactions one can "tag" the interacting photons by detecting the scattered leptons. Three different kinematical conditions, such as double tag, single tag, and no tag, can be distinguished and should be discussed separately. However, we are interested
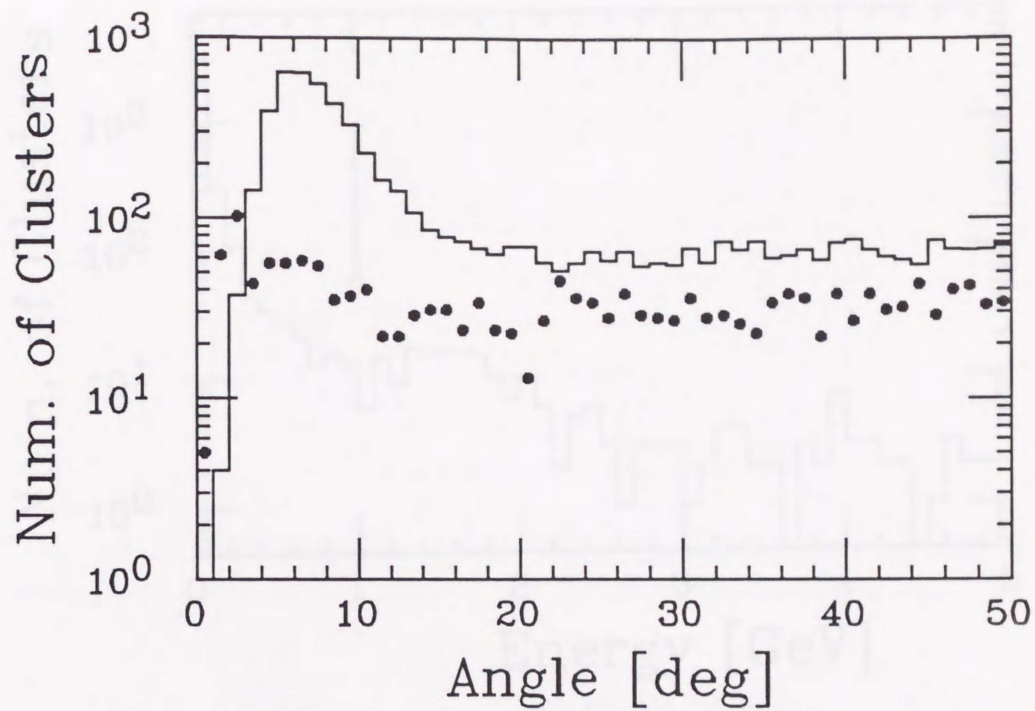
Figure 5.4: The opening angle distribution of neutral shower cluster in the barrel calorimeter is shown, where the opening angle is measured from the nearest lepton track. The histogram indicates electron-pair, whereas and the point indicates muon-pair.
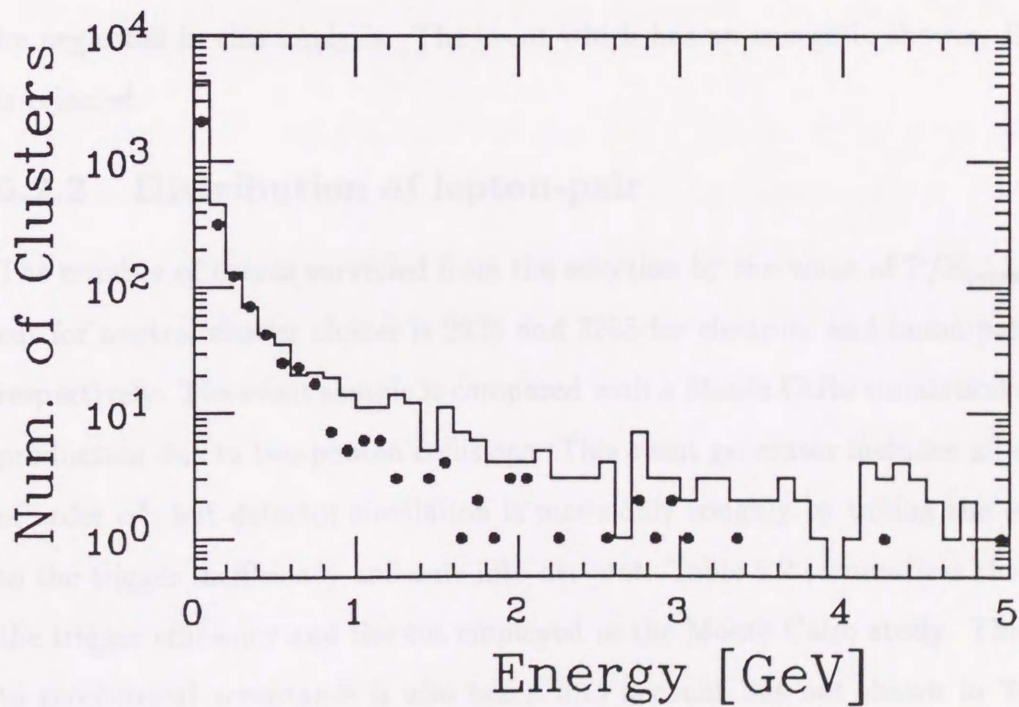
Figure 5.5: Distribution of the energy deposit of neutral clusters with their opening angle being greater than 15°, measured by the barrel calorimeter. The histogram indicates electron-pair and the point indicates muon-pair.
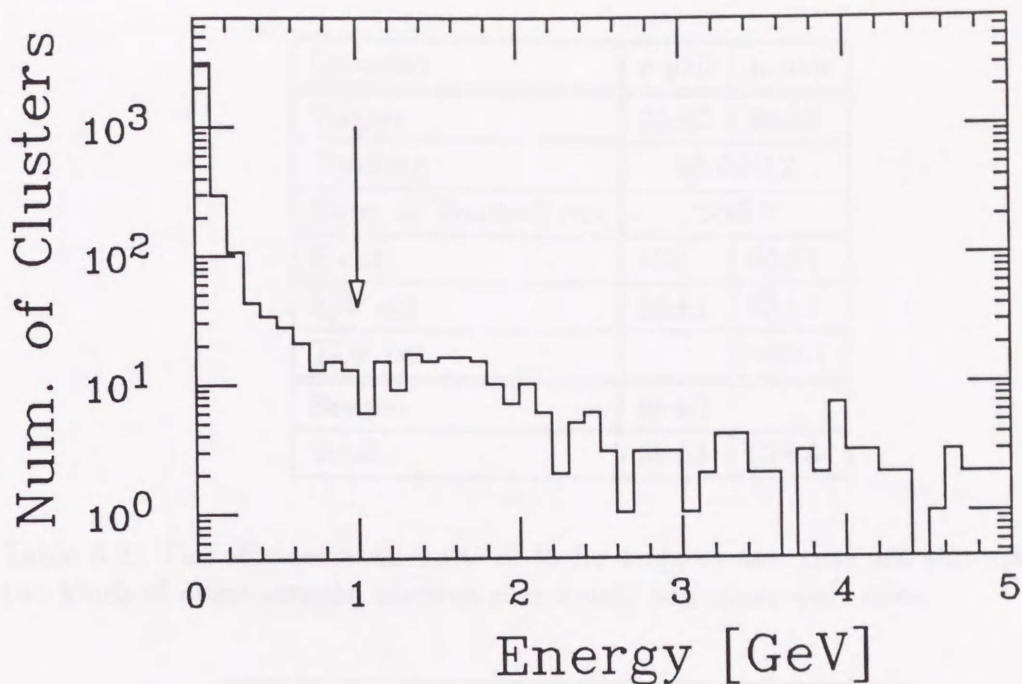
Figure 5.6: The deposit energy of neutal cluster in the end-cap calorimeter. Two types of events, electron-pair and muon-pair, are treated. The arrow corresponds to E=1GeV.

in two-photon interactions as only background to a SUSY event, tagged event can be neglected in this analysis. The event which has an energetic shower, E>1GeV, is rejected.

5.2.2 Distribution of lepton-pair

The number of events survivied from the selection by the value of P/E_{beam} and the cut for neutral shower cluster is 2925 and 3288 for electron- and muon-pair events, respectively. The event sample is compared with a Monte Carlo simulation of lepton production due to two-photon collisions. This event generator includes all diagrams of order α^4, but detector simulation is made only roughly by taking the effect due to the trigger inefficiency and cuts into account. Table 5.2 summarizes the value of the trigger efficiency and the cut employed in the Monte Calro study. The cut due to geometrical acceptance is also taken into account but not shown in Table 5.2. The measured cross sections for $e^+e^- \rightarrow e^+e^-e^+e^-$ and $e^+e^- \rightarrow e^+e^-\mu^+\mu^-$ are shown in Table 5.3, where the values obtained from the Monte Calro simulation

Quantity	e-pair	μ-pair
Trigger	95±2	94±2
Tracking	99.0±0.2	
Num. of Track=2 cut	>99.9	
E cut	100	99±1
E/P cut	96±1	99±1
TOF cut		>99.7
Bremss	95±2	
Total	86±3	92±3

Table 5.2: The efficiencies in units of % for triggers and cuts are summarized for two kinds of event sample, electron-pair events and muon-pair ones.

Process	Measured	MC
$e^+e^- \rightarrow e^+e^-e^+e^-$	$130 \pm 2 \pm 6$	$128 \pm 1 \pm 4$
$e^+e^- \rightarrow e^+e^-\mu^+\mu^-$	$184 \pm 4 \pm 11$	$172 \pm 2 \pm 5$

Table 5.3: Cross section for $e^+e^- \rightarrow e^+e^-e^+e^-$ and $e^+e^- \rightarrow e^+e^-\mu^+\mu^-$ in units of pb. The results by the Monte Carlo study are compared. The errors due to statistical and systematical are indicated separately in that order.

are also shown for comparison. The observed values are in good agreement with the expectations. The systematical errors include uncertainties in the detection efficiency, lumininosity measurement, and background subtraction. Fig. 5.7 shows distributions of transverse momentum measured with respect to the beam axis for lepton tracks. The distributions are in good agreement with the expectation of the Monte Carlo study. The distribution for invariant mass of lepton-pair are shown in Fig. 5.8. The invariant mass is calculated from momentum of lepton-pair. In the low inavariant mass region around 2GeV, the data of both electron and muon are different from the expectation, due to the cut effects, such as E and and P_t, and non-gaussian tail effect in the momentum resolution. Fig. 5.9 indicates the distrbution of the acoplanarity. This is in good agreement with the expectaion. The
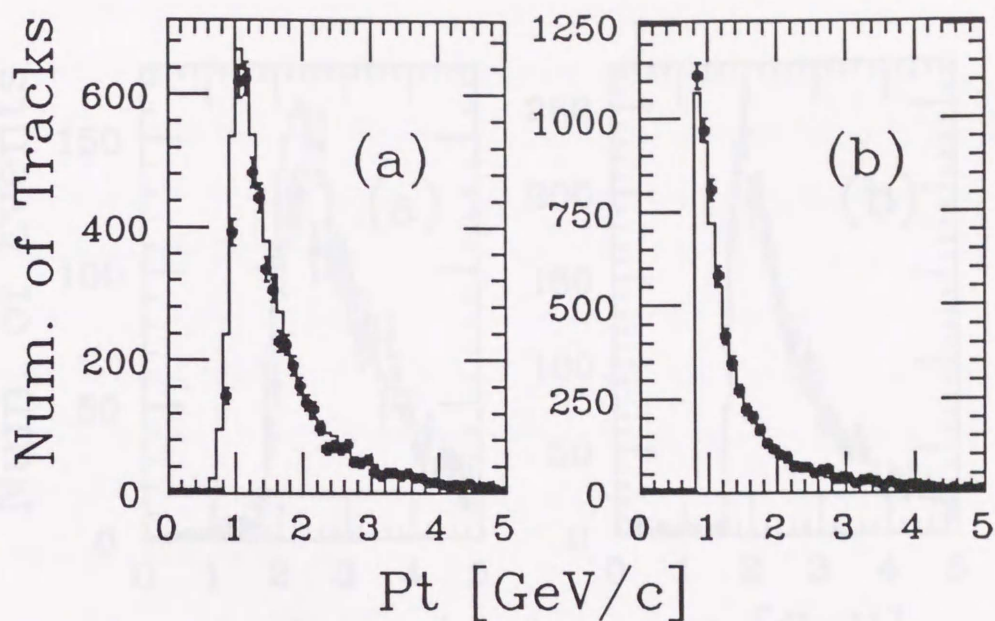
Figure 5.7: Transverse momentum distribution of lepton track. (a):for $e^+e^- \rightarrow e^+e^-e^+e^-$. (b):for $e^+e^- \rightarrow e^+e^-\mu^+\mu^-$ Plot with error bar indicates the data and solid histogram shows the expectation by Monte calro study.

forward-backward asymmetry is given by

$$A_{FB} = \frac{N_F - N_B}{N_F + N_B},$$

where N_F and N_B are the number of tracks in forward and backward hemisphere, respectively. The asymmetry of electron-pair and muon-pair is 0.3 ± 1.4 and $1.0 \pm 1.2\%$, respectively, and are consistent with 0 as to be expected.

From these facts one may say that the efficiencies in Table 5.2 and other cuts are evaluated correctly and we can safely use these efficiencies in searching for SUSY particles in the next section.

5.3   Search for superpartner

The signature of SUSY partner event is impressive, because they have a certain missing energy and an unbalanced topology. Our search is made in the following two ways: One is the case in which $\tilde{\ell}$ decays into photino and ordinary lepton, where photino is the LSP. The event of this process has a certain amount of missing energy since photino can only weakly interact with detector materials and may presmably
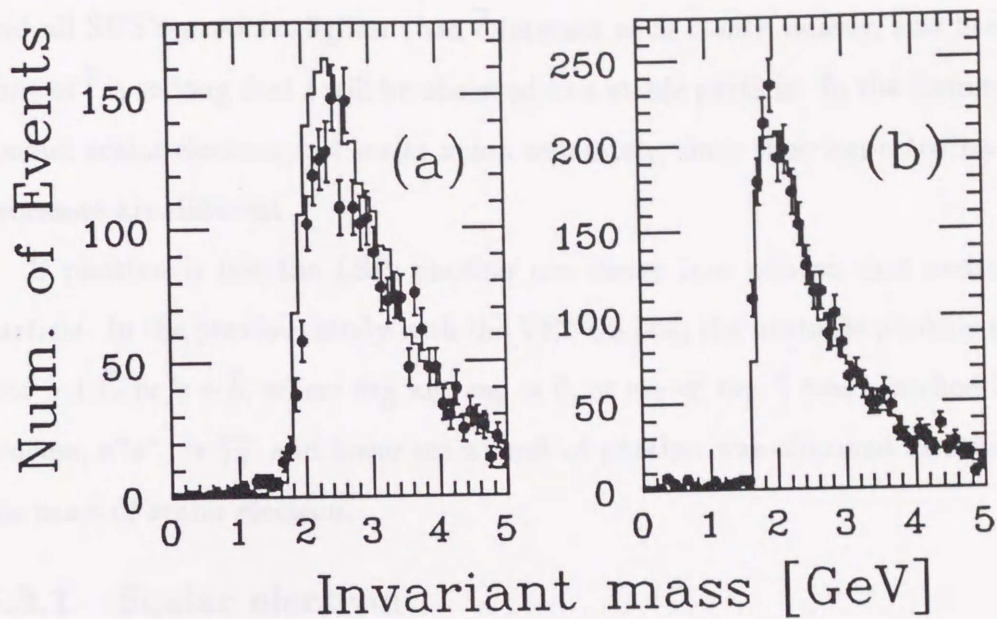
Figure 5.8: Invariant mass distribution of lepton-pair. (a):for $e^+e^- \to e^+e^-e^+e^-$. (b):for $e^+e^- \to e^+e^-\mu^+\mu^-$. The point with error bar indicates the data and the solid histogram shows the expectation of the Monte Carlo study.
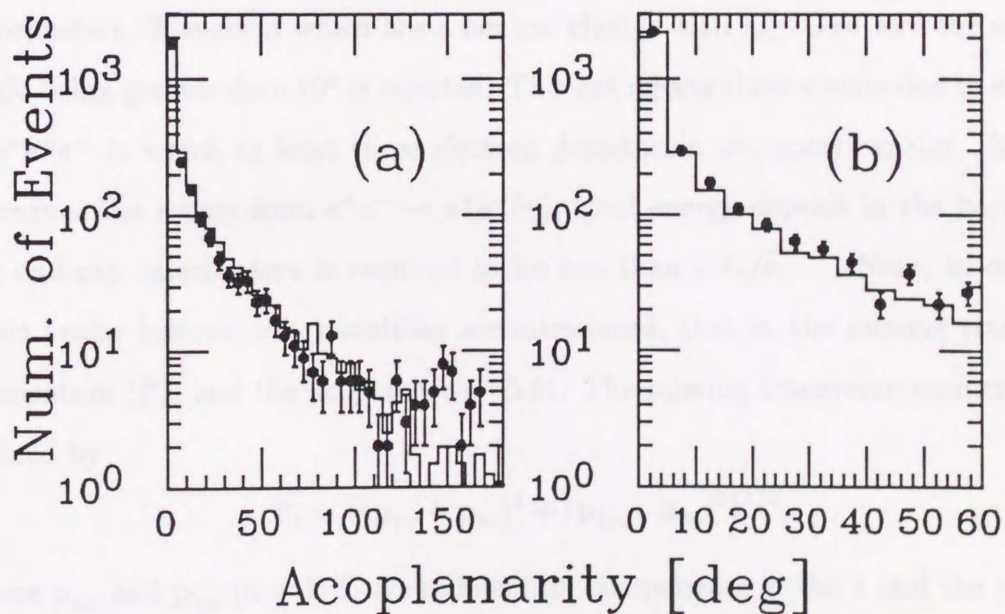
Figure 5.9: Acoplanarity distribution of lepton pair. (a):for $e^+e^- \to e^+e^-e^+e^-$. (b):for $e^+e^- \to e^+e^-\mu^+\mu^-$ The pointt with error bar indicates the data and the solid histogram shows the expectation of the Monte Carlo study.

escape from the detector. The other is the case in which $\widetilde{\ell}$ is heavier than photino and all SUSY-particles lighter than $\widetilde{\ell}$ interact with $\widetilde{\ell}$ only weakly, and here the life time of $\widetilde{\ell}$ is so long that $\widetilde{\ell}$ will be observed as a stable particle. In the former case, we discuss scalar electron and scalar muon separately, since their expected background processes are different.

If photino is not the LSP, photino can decay into photon and neutral SUSY particle. In the previous study with the VENUS [29], the unstable photino (decaying into $\gamma + \widetilde{G}$ or $\gamma + \widetilde{h}$, where $m_{\widetilde{G}}$ and $m_{\widetilde{h}} = 0$, or $m_{\widetilde{h}} \ll m_{\widetilde{\ell}}$.) was searched for in the process, $e^+e^- \to \widetilde{\gamma}\widetilde{\gamma}$, and lower mass limit of photino was obtained as a function of the mass of scalar electron.

5.3.1 Scalar electron

If the LSP is photino, in scalar electron pair production, $e^+e^- \to \widetilde{e}\overline{\widetilde{e}}$, we can detect only electron-pair with a considerable amount of missing energy.

At first, the events which contain only electron-pair are required in the data sample selected in section 4.2. Fig. 5.10 shows the shower energy distribution of the cluster which do not associate with electron track in both of the barrel and end-cap calorimeters. The event which has a neutral cluster with $E \geq 1\,\mathrm{GeV}$ and the opening angle being greater than $10°$ is rejected. This cut rejects these events due to $e^+e^- \to e^+e^-e^+e^-$ in which at least three electron detected in our spectrometer. In order to reduce the events from $e^+e^- \to e^+e^-(\gamma)$, total energy deposit in the barrel and the end-cap calorimeters is required to be less than $0.8\sqrt{s}$. Next, in order to select scalar leptons, two quantities are introduced, that is, the missing transverse momentum ($\not{P}_t$) and the acoplanarity ($\Delta\phi$). The missing transverse momentum is defined by

$$\not{P}_t = \{(\mathbf{p}_{1x} + \mathbf{p}_{2x})^2 + (\mathbf{p}_{1y} + \mathbf{p}_{2y})^2\}^{1/2},$$

where $\mathbf{p}_{nx}$ and $\mathbf{p}_{ny}$ ($n = 1, 2$) are momentum components in the x and the y directions, respectively, measured by the CDC. The acoplanarity ($\Delta\phi$) is defined by

$$\Delta\phi = 180° - \cos^{-1}\left(\frac{(\mathbf{p}_1 \times \hat{\mathbf{z}}) \cdot (\mathbf{p}_2 \times \hat{\mathbf{z}})}{|\mathbf{p}_1 \times \hat{\mathbf{z}}| \cdot |\mathbf{p}_2 \times \hat{\mathbf{z}}|}\right),$$

escape from the detector. The other is the case in which $\tilde{\ell}$ is heavier than photino and all SUSY-particles lighter than $\tilde{\ell}$ interact with $\tilde{\ell}$ only weakly, and here the life time of $\tilde{\ell}$ is so long that $\tilde{\ell}$ will be observed as a stable particle. In the former case, we discuss scalar electron and scalar muon separately, since their expected background processes are different.

If photino is not the LSP, photino can decay into photon and neutral SUSY particle. In the previous study with the VENUS [29], the unstable photino (decaying into $\gamma + \tilde{G}$ or $\gamma + \tilde{h}$, where $m_{\tilde{G}}$ and $m_{\tilde{h}} = 0$, or $m_{\tilde{h}} \ll m_{\tilde{\ell}}$.) was searched for in the process, $e^+e^- \rightarrow \tilde{\gamma}\tilde{\gamma}$, and lower mass limit of photino was obtained as a function of the mass of scalar electron.

5.3.1   Scalar electron

If the LSP is photino, in scalar electron pair production, $e^+e^- \rightarrow \tilde{e}\bar{\tilde{e}}$, we can detect only electron-pair with a considerable amount of missing energy.

At first, the events which contain only electron-pair are required in the data sample selected in section 4.2. Fig. 5.10 shows the shower energy distribution of the cluster which do not associate with electron track in both of the barrel and end-cap calorimeters. The event which has a neutral cluster with E$\geq$1GeV and the opening angle being greater than 10° is rejected. This cut rejects these events due to $e^+e^- \rightarrow e^+e^-e^+e^-$ in which at least three electron detected in our spectrometer. In order to reduce the events from $e^+e^- \rightarrow e^+e^-(\gamma)$, total energy deposit in the barrel and the end-cap calorimeters is required to be less than $0.8\sqrt{s}$.   Next, in order to select scalar leptons, two quantities are introduced, that is, the missing transverse momentum ($\not{P}_t$) and the acoplanarity ($\Delta\phi$). The missing transverse momentum is defined by

$$\not{P}_t = \{(p_{1x} + p_{2x})^2 + (p_{1y} + p_{2y})^2\}^{1/2},$$

where $\mathbf{p}_{nx}$ and $\mathbf{p}_{ny}$ ($n = 1, 2$) are momentum components in the x and the y directions, respectively, measured by the CDC. The acoplanarity ($\Delta\phi$) is defined by

$$\Delta\phi = 180° - \cos^{-1}\left(\frac{(\mathbf{p}_1 \times \hat{\mathbf{z}}) \cdot (\mathbf{p}_2 \times \hat{\mathbf{z}})}{|\mathbf{p}_1 \times \hat{\mathbf{z}}| \cdot |\mathbf{p}_2 \times \hat{\mathbf{z}}|}\right),$$

65

where $\mathbf{p}_1$ and $\mathbf{p}_2$ are the 3-dimensional momentum vector of tracks 1 and 2, respectively, $\hat{\mathbf{z}}$ is the unit vector in the direction of beam axis. A scatter plot of missing transverse momentum vs acoplanarity is shown in Fig. 5.11. The acoplanarity distribution of the selected events is plotted in Fig. 5.12. The contributions from the known processes, $e^+e^- \rightarrow e^+e^-e^+e^-$, $e^+e^- \rightarrow e^+e^-\tau^+\tau^-$, $e^+e^- \rightarrow e^+e^-(\gamma)$, and $e^+e^- \rightarrow \tau^+\tau^-(\gamma)$, are estimated with Monte Carlo methods including a full detector simulation. The expected acoplanarity distribution is shown by the solid histogram in Fig. 5.12. Both of the observed and expected distributions extend to the larger acoplanarity region, and a good agreement between them can be seen.

In order to discriminate the e^+e^- events from scalar electron-pair production, we apply the following cuts: $\Delta\phi \geq 20°$ and $\not{P}_t \geq 4.5$ GeV/c. The acoplanarity distribution after the $\not{P}_t$ cut is shown by the dashed histogram in Fig. 5.12. No event remains after these cuts. The trigger efficiency for the events that survive the cuts is more 99% because they are redundantly triggered by the total energy trigger for the LG calorimeter ($E \geq 4$ GeV) as well as the segment sum trigger of the LG calorimeter. The overall detection efficiency is expected to be 89±3% for such events when the effect of an E/P cut, the inefficiency due to bremsstrahlung (1.5±1%) and hard photon emision (1.9±1%) is taken into account. The expected number of events for scalar electron-pair production is estimated for two different cases, namely, the masses in question have a large splitting, or are degenerate, with various combinations of $m_{\tilde{e}}$ and $m_{\tilde{\gamma}}$, where the effect of initial-state radiations is taken into account in a classical manner[30]. Monte Carlo methods including only a detector acceptance simulation and the overall detection efficiency are carried out for these combinations. The uncertainty in this expectation is estimated to be 5% in total, including the uncertainties in the detection efficiency and the luminosity measurement. In order to make the estimation rather conservative, the expected value is always reduced by 5%. Then, the present observation of no event after the final cuts allows us to exclude the regions shown in Fig.5.13 at the 95% confidence level (c.l.). For $m_{\tilde{\gamma}} = 15$ GeV/c^2, the large splitting (degenerate) scalar electrons are excluded between 16.5 (16.1) GeV/c^2 and 28.5 (30.5) GeV/c^2 at 95% c.l.

5.3.2 Scalar muon

At first the event which has a neutral shower energy deposit, E$\geq$1GeV in the barrel and the end-cap calorimeters is rejected, similar to the case of scalar electron. The overall detection effieciency is estimated to be 92$\pm$2% for the muon-pair event sample selected in section 4.3. A scatter plot of missing transverse momentum vs acoplanarity for muon-pair events is shown in Fig. 5.14. The acoplanarity distribution for the selected events is shown in Fig. 5.15, where a comparison is made with the expected contributions from the known processes (solid histogram): $e^+e^- \rightarrow e^+e^-\mu^+\mu^-$, $e^+e^- \rightarrow e^+e^-\tau^+\tau^-$, $e^+e^- \rightarrow \mu^+\mu^-(\gamma)$, $e^+e^- \rightarrow \tau^+\tau^-(\gamma)$, and $e^+e^- \rightarrow e^+e^-$+hadrons. The observation is in good agreement with the expectation.

The muon-pair from scalar muon pair production is examined by applying the cuts: $\Delta\phi \geq 15°$ and $\not{P}_t \geq 4.0$ GeV/c. The acoplanarity distribution after the $\not{P}_t$ cut is shown by the dashed histogram in Fig. 5.15. One event which is in Fig. 5.16 survives through the final cuts. This event has such topology as $\not{P}_t = 10.1$ GeV/c and $\Delta\phi = 15.05°$. The corresponding number of expected events for the known processes is estimated to be 0.1. We consider that this event comes from τ-pair production and the excess in $\Delta\phi$ value is due to the finite momentum resolution. One of tracks in this event has large P_t, 11.3 GeV/c and this gives an error of $\not{P}_t$ of 1 GeV/c. We analyze that this event is regared as SUSY one when the mass limit is obtained.

The number of expected events for scalar muon prodution is estimated by taking the detection efficiency into account. The effect of initial-state radiations is included according to Berends and Kleiss[33]. We always underestimate the expected values by 5%, taking the errors in the detection efficiency and luminosity measurement into account. Then the present observation of one event may be translated to the excluded regions (95% c.l.) shown in Fig. 5.17. For $m_{\tilde{\gamma}} = 0$, the large-splitting (degenerate) scalar muons are excluded at 2.6 (1.9) $< m_{\tilde{\mu}} <$ 22.9 (25.2) GeV/c^2.

5.3.3 Stable charged scalar particle

Fig. 5.18 shows the distribution of the inverse velocity, $1/\beta$, which is obtained from the track length and the time-of-flight for the tarcks selected in section 4.4. The track length is calculated from the tracking information in the CDC. All selected tracks distribute around $1/\beta = 1$ and no evidence is found for slow particle pair-production. When the final cut $1/\beta > 1.2$, no event remains. The cut value, $1/\beta = 1.2$, corresponds to a particle mass of about 17 GeV/c^2 at $\sqrt{s}$ =61.4GeV. Since stable charged scalar production is already excluded up to 24 GeV/c^2 in the previous e^+e^- colliding experiment[28], only the upper bound of the excluded region is important in this analysis.

The overall detection efficiency is estimated to be 87±2% for any charged-particle pairs when the effect of the acceptance cuts, the trigger efficiency, and the inefficiency due to the requirements on time-of-flight measurements is taken into account. Sensitivity of this search to heavy particles may be limited by the energy-loss of the particles in detector-materials. The materials from the beam-pipe up to the middle of the TOF counters correspond to 5 g/cm^2, where the dominant constituents are aluminum and carbon. Even if we take acount of the effect of production polar-angle and bending by the magnetic field, the effective material thickness never exceeds 10 g/cm^2 for any particles. If $1/\beta < 5$, which corresponds to a particle heavier than 20GeV/c^2, the particle easily penetrates the detector materials to reach the middle of the TOF counters and leave signals. By taking the detection efficiency and velocity cut-off, $1/\beta < 5$, into account, the observation of no candidate for heavy particle allows us to exclude the large-spiltting (degenerate) scalar-muons and scalar-taus with masses smaller than 28.1 (29.0) GeV/c^2 at the 95% confidence level.

For large-splitting scalar-electron, the lower limit is 28.4 GeV/c^2 if $M_{\tilde{\gamma}} = M_{\tilde{e}}$. The limit decrease with the photino-mass and reaches a minimum of 27.3 GeV/c^2 around $M_{\tilde{e}} = 50$ GeV/c^2. Thus, the limit independent of the photino-mass is 27.3 GeV/c^2. For the degenerate scalar electrons, the lower limit is determined by the velocity cut-off for the data (5.1 pb^{-1}) with $\sqrt{s}$ =61.4 GeV to be 30.2 GeV/c^2 up to $M_{\tilde{\gamma}} = 145$ GeV/c^2. Above that, the limit decrease with the photino-mass,

approaching to the limit for scalar-muons and scalar-taus, 29.0 GeV/c^2, at M$_{\tilde{\gamma}}$ = O(1 TeV/c^2). If we assume the products are fermions with a unit charge (heavy leptons, charginos and so on), the mass-limit is totally determined by the velocity cut-off. As a results of this, the mass lower-limit for stable fermions is improved to be 29.5 GeV/c^2.

Figure 5.10: Distribution of shower energy for neutral clusters in the barrel and end-cap calorimeter.
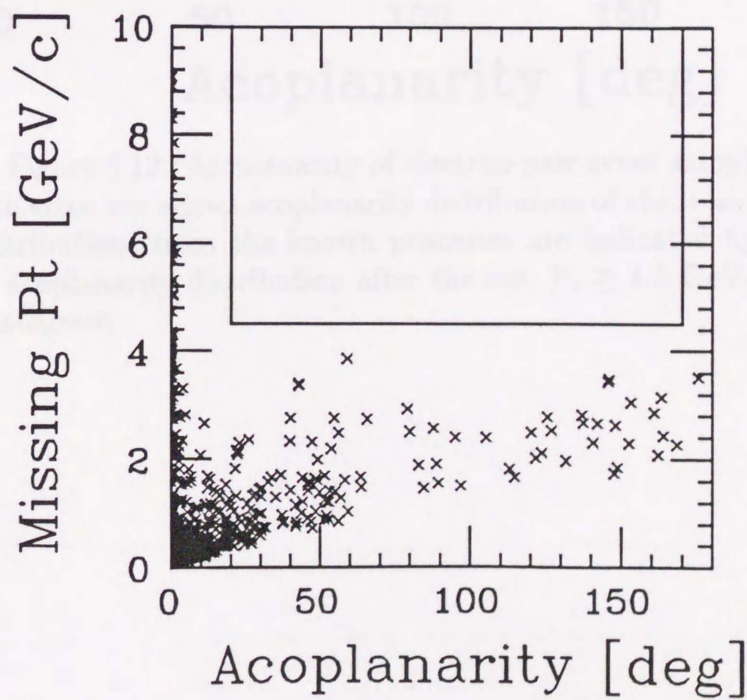
Figure 5.11: P_t vs acoplanarity of electronvent saansevermple
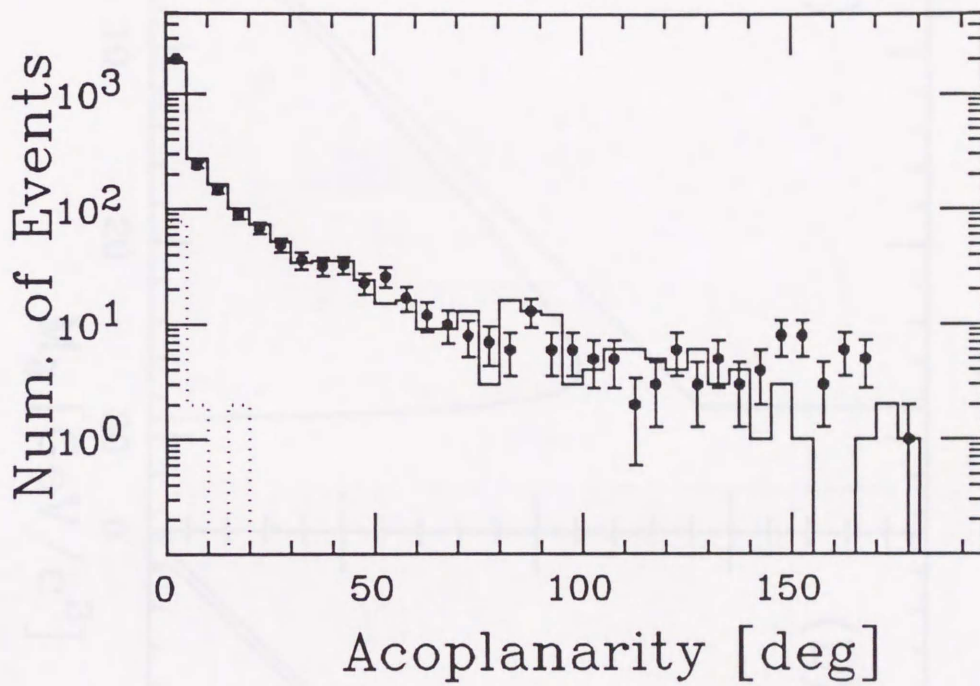
Figure 5.12: Acoplanarity of electron-pair event sample
The point with error bar shows acoplanarity distribution of electron-pair event sample. The contributions from the known processes are indicated by the solid histogram. The acoplanarity distribution after the cut, $P_t \geq 4.5$ GeV/c, is shown by the dashed histogram
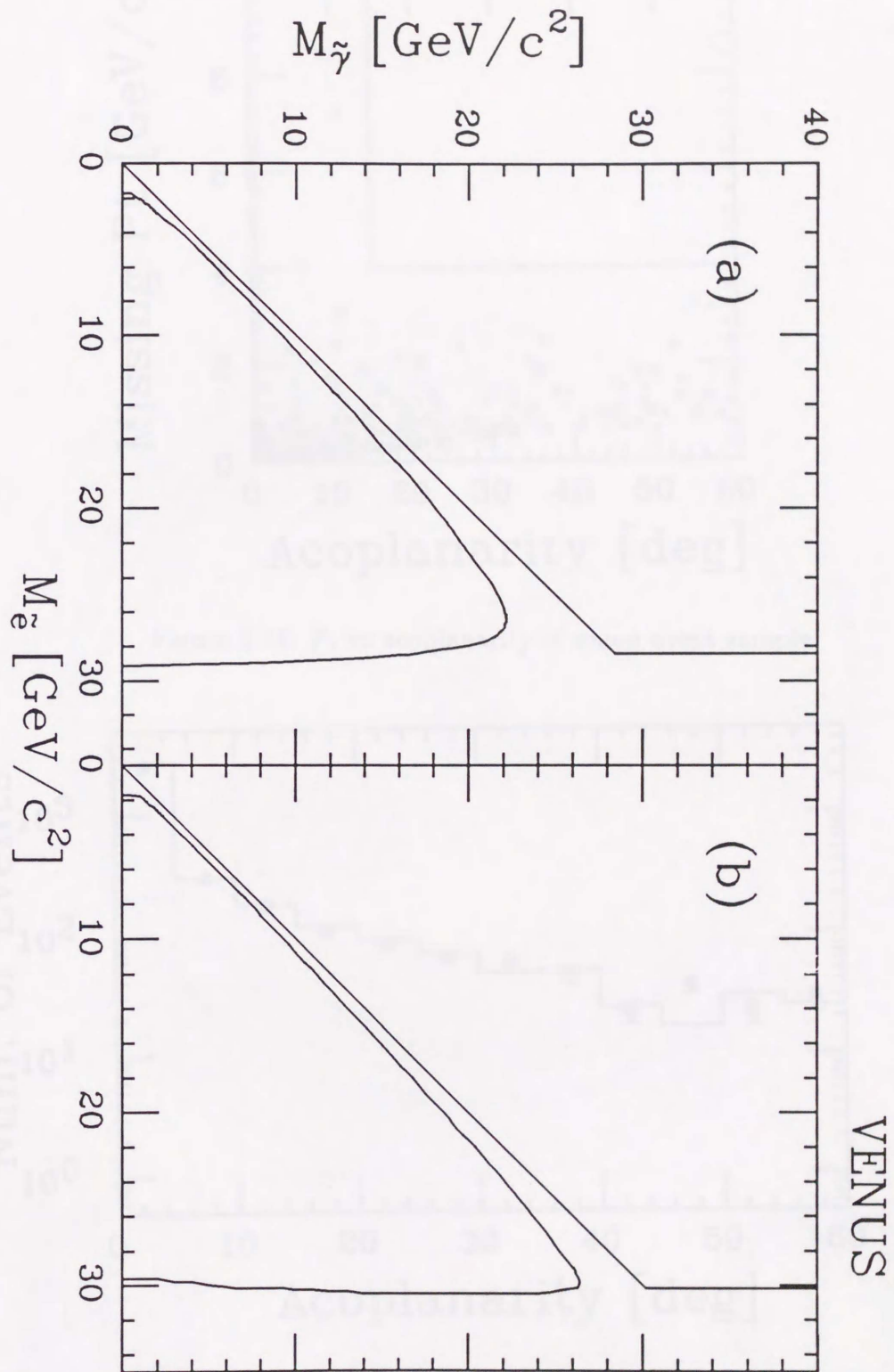
Figure 5.13: Scalar electron mass limits at 95% confidence level. (a):large mass splitting case, (b):mass degenerate case.
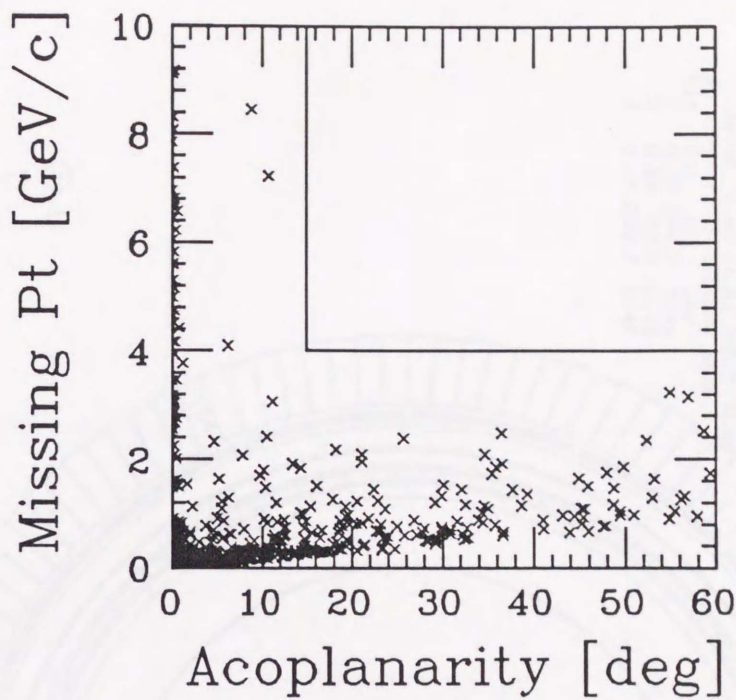
Figure 5.14: $\not{P}_t$ vs acoplanarity of muon event sample
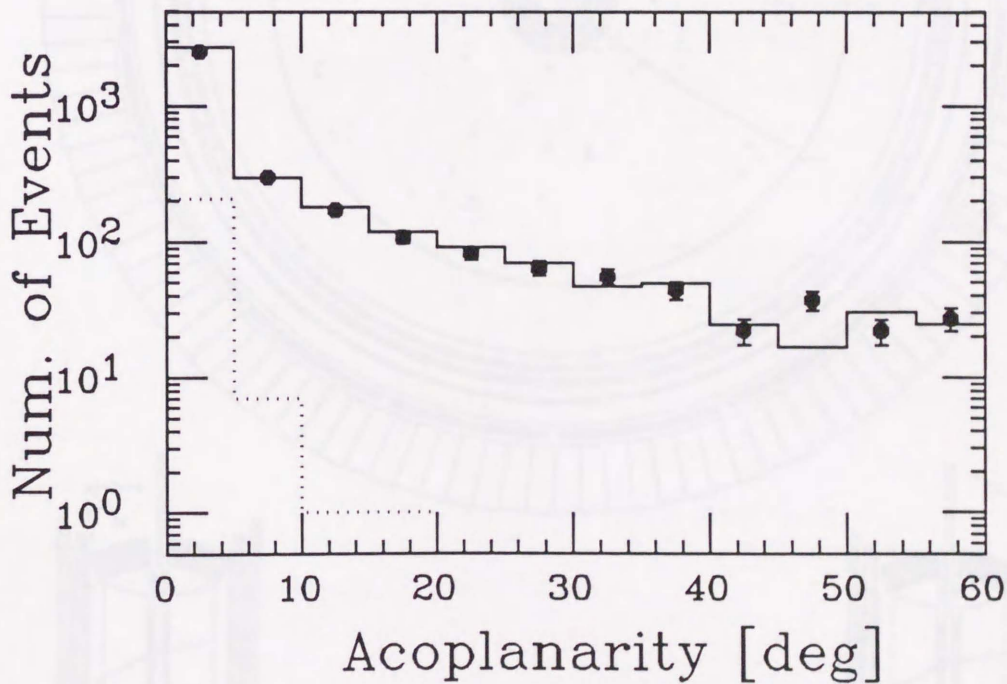
Figure 5.15: Acoplanarity of muon-pair event sample

The point with error bar shows acoplanarity distribution of muon-pair event sample. The contributions from known processes are indicated by the solid histogram. The acoplanarity distribution after the cut, $\not{P}_t \geq 4.0$ GeV/c, is shown by the dashed histogram
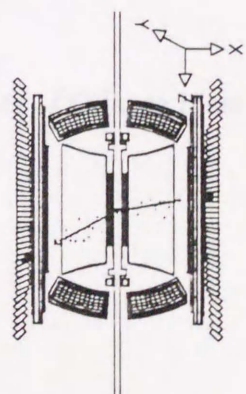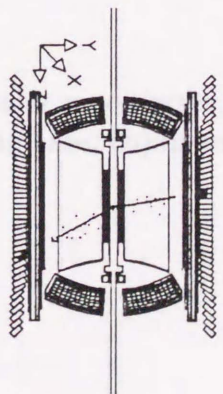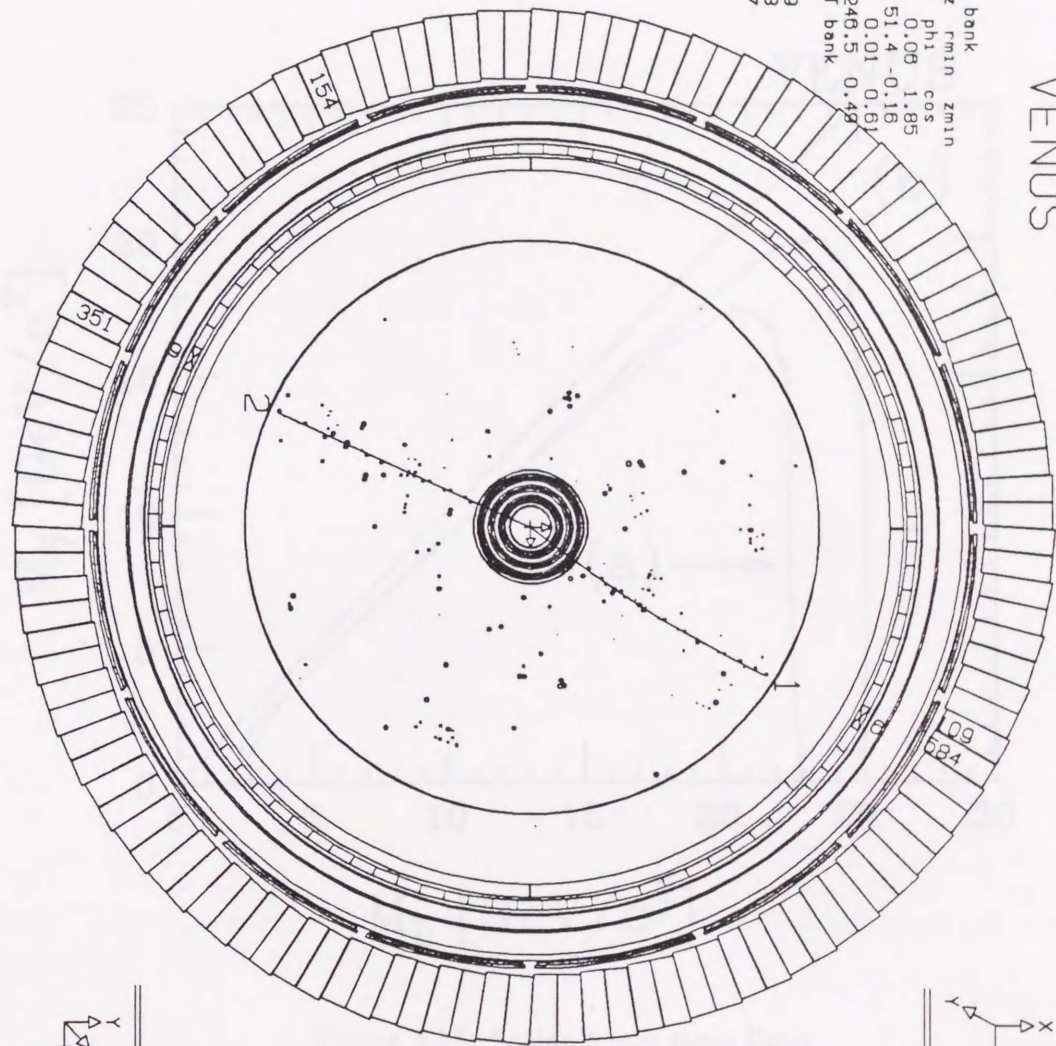
Figure 5.16: Survived event from scalar muon selection

74
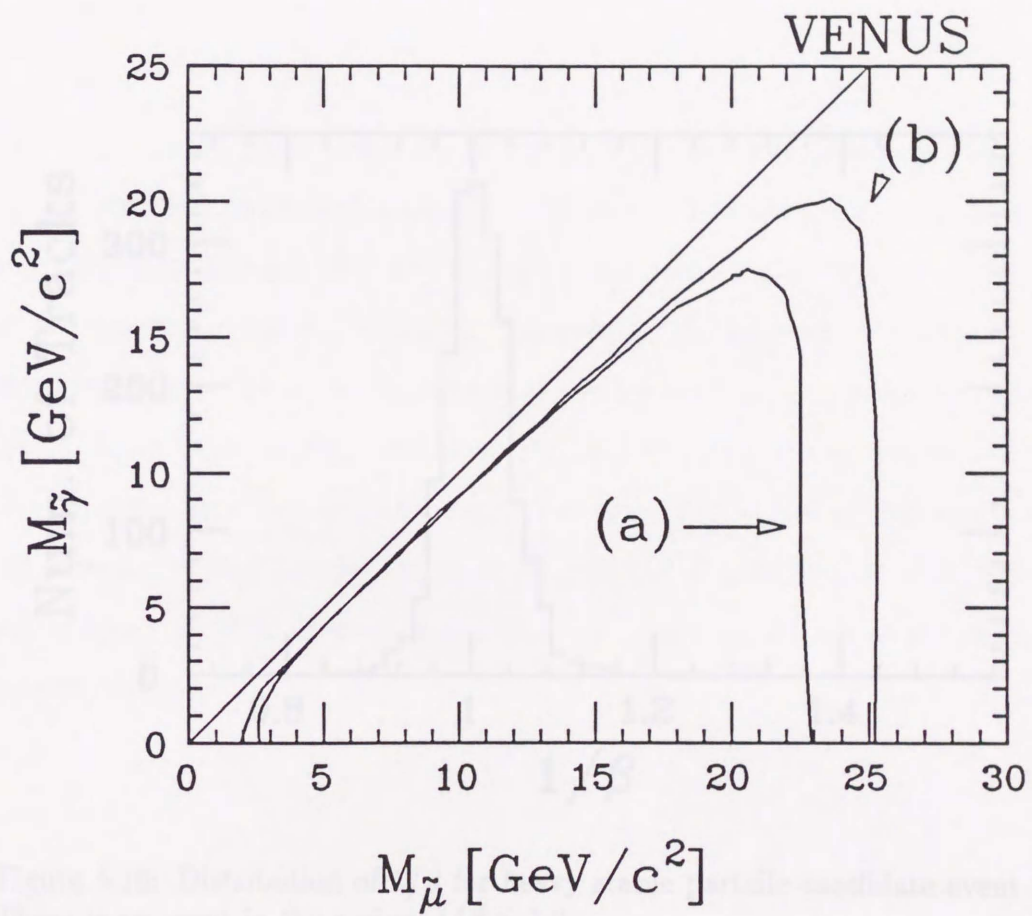
Figure 5.17: Scalar muon mass limit
Scalar muon mass limits at 95% confidence level are indicated. (a):large mass splitting case, (b):mass degenerate case.
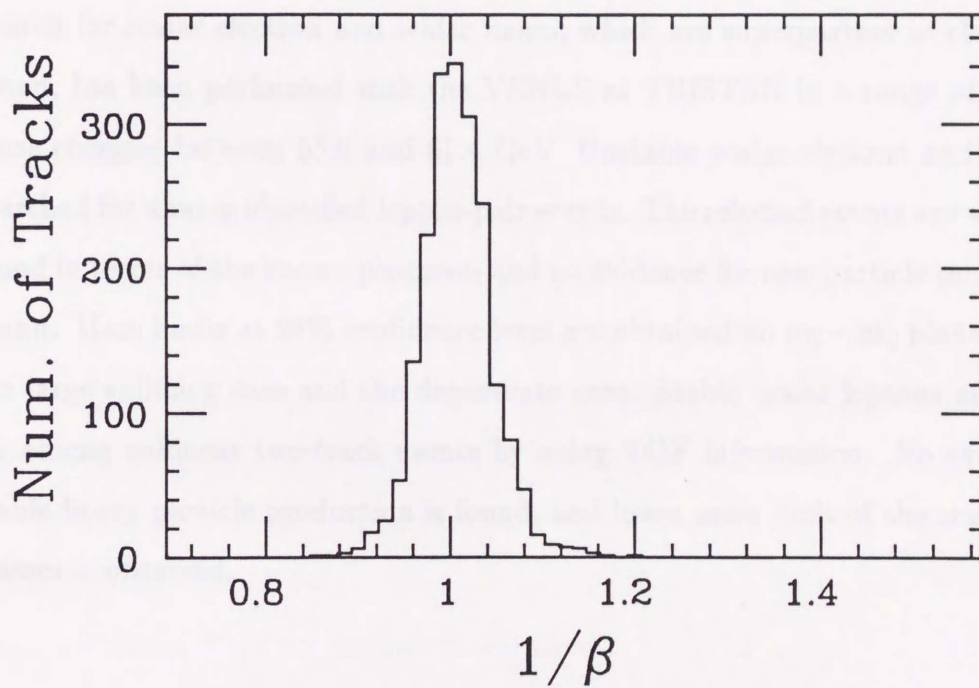
Figure 5.18: Distribution of $1/\beta$ for heavy stable partcile candidate event sample. There is no event in the region, $1/\beta > 1.2$.

Chapter 6
Conclusion

Search for scalar electron and scalar muon, which are superpartner of electron and muon, has been performed with the VENUS at TRISTAN in a range of center-of-mass energies between 55.0 and 61.4 GeV. Unstable scalar electron and muon are searched for among identified lepton-pair events. The selected events are well understood in terms of the known processes and no evidence for new particle production is found. Mass limits at 95% confidence level are obtained on $m_{\tilde{\ell}}$ – $m_{\tilde{\gamma}}$ planes for both the large splitting case and the degenerate case. Stable scalar leptons are selected for among collinear two-track events by using TOF information. No evidence for stable heavy particle production is found, and lower mass limit of the scalar lepton masses is obtained.

Acknowledgements

The work described in this thesis is due to the efforts of a large number of people, all of whom must receive my thanks. The success of the experiment is the result of the dedicated effort of all the members of the VENUS Collaboration and the TRISTAN machine group.

I am most indebted to my supervisor Prof. Y. Sumi, for his continual support and guidance. In this thesis there are large amount of his comments and suggestions. I would like to acknowledge to Prof. T. Ohsugi for his continuous encouragement and support during the study in the graduate course. I wish to thank all of the members of my laboratory for their continuous help.

I would like to thank Dr. S. Uehara, Dr. S. Odaka, and Dr. T. Tuboyama for discussing my analysis and for many criticisms and suggestions. Dr. H. Sakamoto, Dr. Y. Arai and Dr. H. Kurashige are greatly acknowledged for their guidance during the work to upgrade the trigger system.

I acknowledge the late Prof. T. Kittaka in Okayama University who taught me very charm of physics and guided me to the field of experimental physics.

Most of all, I would like to thank my parents and family for their continuous support during the graduate course of study at Hiroshima University. Without their help, my thesis could not have been finished.

Bibliography

[1] E.Leader et al., An introduction to gauge theories and the new physics, Cambridge University Press, Cambridge, 1982

[2] P.W.B.Higgs, Phys. Lett. **12**,132,1964

[3] J.Wess et al., Nucl. Phys. **B70**(1974)39

[4] F.A.Berends et al., Nucl. Phys. **B253**(1985)441

[5] I.Hayashibara et al., Phys. Lett. **B158**(1985)349

[6] T.Kobayashi et al., Phys. Lett. **B134**(1984)271

[7] M.Gluck et al., Phys. Lett. **B130**(1983)423

[8] H.E.Harber et al., Phys. Rep. 117, 75, 1985.

[9] TRISTAN project group, KEK Report 86-14, (1987)

[10] J. Iwahori et al., VENUS proposal KEK report(1983)

[11] M. Shioden, Ph. D. Thesis, University of Tsukuba (1988) unpublished

[12] K.Kubo, Ph. D. Thesis, Kyoto University (1988) unpublished

[13] R. Arai et al., Nucl. Instr. Meth. **217**(1983)181

[14] F. Suekane et al., IEEE Trans. Nucl. Sci. **33**(1986)73

[15] M. Ikeno et al., IEEE Trans. Nucl. Sci. **33**(1986)779

[16] T. Ohsugi et al., Nucl. Instr. Meth. **A269**(1988)522

[17] Y. Hemmi et al., Jpn. Appl. Phys. **26**(1987)982

[18] H. Kurashige et al., IEEE Trans. Nucl. Sci. **35**(1988)1018

[19] O. Sasaki et al., IEEE Trans. Nucl. Sci. **35**(1988)342

[20] R. Arai et al., Nucl. Instr. Meth. **A254**(1988)433

[21] T. Sumiyoshi et al., Nucl. Instr. Meth. **A271**(1988)432

[22] M. Sakano, Ph. D. Thesis, University of Tsukuba (1988) unpublished

[23] H. Saito et al., Nucl. Instr. Meth. **A270**(1988)219

[24] Y.Arai Private comminucation

[25] Y. Yasu et al., IEEE Trans. Nucl. Sci. **31**(1984)197

[26] Y. Chiba et al., Nucl. Instr. Meth. **A269**(1988)171

[27] T.Oyama, Master Thesis, Tokyo Metropolitan University (1988) unpublished

[28] I.Adachi et al., Phys. Lett. **218B**(1989)105

[29] The VENUS Collaboration, Zeit. Physik **C45**(1989)175

[30] E.Etim et al., Nuovo Cimento **B51**(1967)276;
    G.Pancheri et al., Nuovo Cimento **A60**(1969)321

[31] K.Abe et al., J. Phys. Soc **56**(1987)3767

[32] K.Tobimatsu et al., Prog. Theor. Phys. **74**(1985)567; **75**(1986)905;
    76(1986)334;
    S.Kuroda et al., Comput. Phys. Commun. **48**(1988)335

[33] F.A.Berends et al., Nucl. Phys. **B178**(1981)141

[34] M.Igarashi et al., Nucl .Phys. **B263**(1086)347

[35] F.A.Berends et al., Nucl. Phys. **253**(1985)441
    F.A.Berends et al., Comput. Phys. **40**(1986)285

[36] R.P.Johnson, SLAC Report 294(1988)

[37] H.Kolanoski, Two-Photon Physics at e^+e^- Storage Rings, Springer-Verlag, Berlin (1984)

[38] T.Kamitani, Ph. D. Thesis, Osaka University (1989) unpublished

[39] The VENUS Collaboration, To be published in Zeit. Physik

Appendix A
Look-up table

Fig. A.1 shows the principle of the look-up table. One has to prepare a size of memory modules large enough to cover the number of signal inputs. The input signals are supplied to address lines of these memories with timing signal, and then the track flag written in advance comes out as a memory readout action. If one wants

RAM

Input signals

Address lines

Output

Trigger out

Read out gate
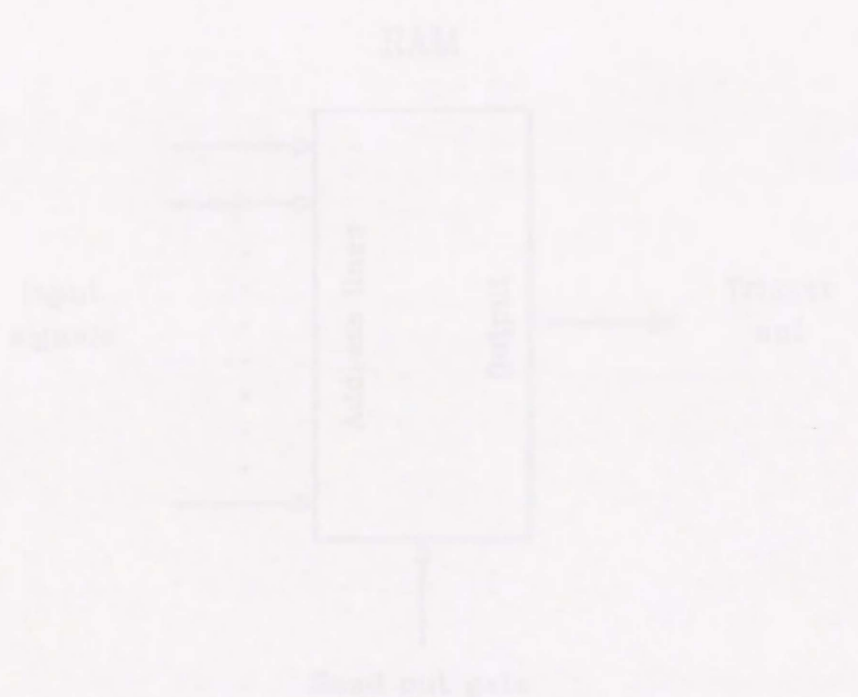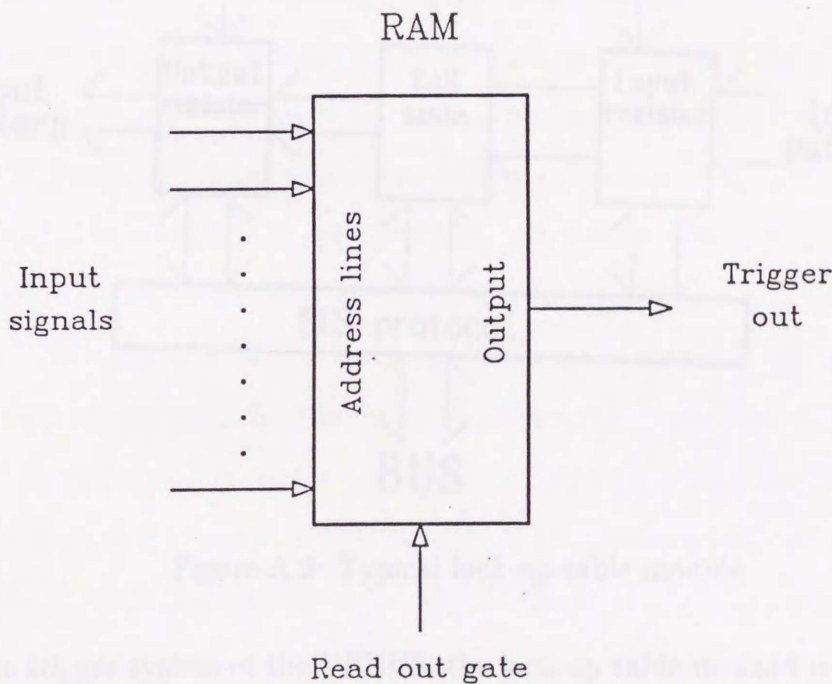
Figure A.1: Principle of the look-up table for track finding

to make up such a naive look-up table, one needs an enormous number of memories. For example, processing of only 64 signal inputs requires a 2^{64}-bit table which is obviously impossible to be implemented. However, if we look at the table contents carefully, most of area of the naive look-up table is found to be empty space. Only

some of special combinations of the input signals are realized and other combinations never come up in practical use. Such specific combinations could be selected out analytically or by a Monte Carlo simulation. We classify the selected combinations to specific clusters so that the number of input signals forming the combinations is equal to or less than the number of address lines of available memory chip. The required look-up table can be made up with this memory chip. Thus how to make a grouping of input signals is the most critical point in designing the look-up table. Fig. A.2 shows the block diagram of the typical look-up table module. The module consists of static RAMs, protocol circuits in order to write RAM contents and a timing control circuit.
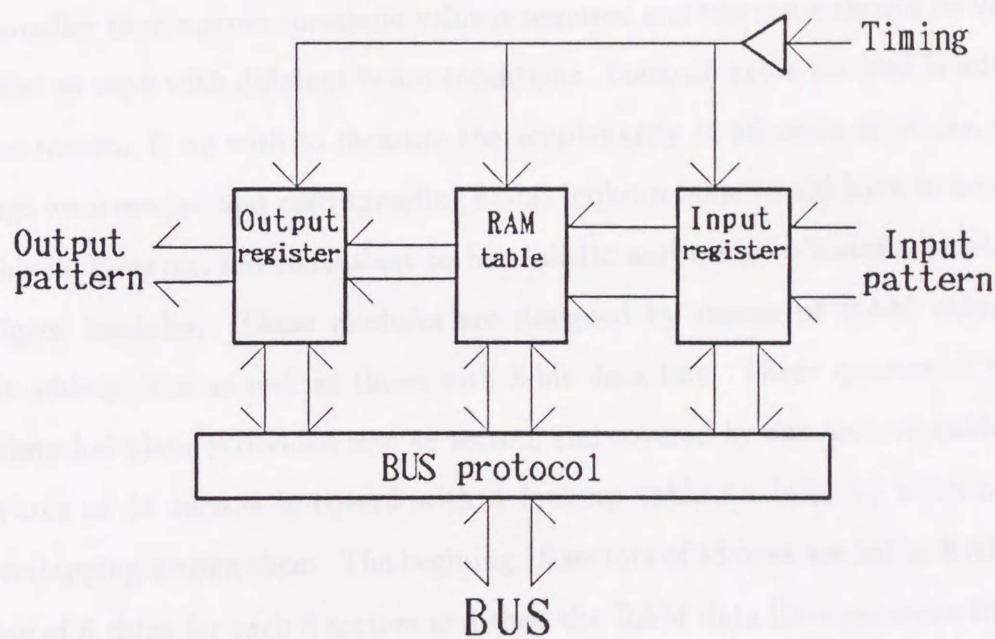
Figure A.2: Typical look-up table module

In the trigger system of the VENUS, the look-up table method is used for track finding in the IC and the CDC, and for track pair search requires some geomemetrical coincidence in the TTL trigger.

The track finding modules specified for the VENUS CDC are made and checked their reliabilty. Their error rate is less than 10^{-10} for look-up table readout emulating the triggering operation for the VENUS.

Appendix B

Two-track limited trigger modules

For the two-track limited (TTL) trigger, at least a pair of tracks whose acoplanarity is smaller than a given threshold value is required and the value should be variable in order to cope with different beam conditions. Look-up table method is adopted for this reason. If we wish to measure the acoplanarity of all pairs of tracks, 64-sector flags were needed and corresponding 64-bit look-up table would have to be designed. This is, however, too redundant to be realistic and we have instead developd TTL trigger modules. These modules are designed by means of RAM chips with 8-bit address line as well as those with 8-bit data line. Three quarter of the whole azimuthal plane is divided into 48 sectors and covered by one look-up table module. Whole of 64 sectors is coverd with 4 look-up table modules by allowing enough overlapping among them. The begining 16 sectors of 48 ones are fed to RAM address line of 8 chips for each 8 sectors and then the RAM data lines generate the 48 flags corresponding to the sectors which satisfy the acoplanarity requirement from input 16 sectors. The 48 flags are coincided with input 48 sector flags. The coincided flag means that a pair of tracks satisfies the required acoplanarity constraint. Total 48 sectors × 4 modules coincided flags are ORed into one signal and then the signal is send to the TDM as the TTL trigger signal. This system consists of the following three types of modules:

1. Signal distributor of 64-sector flag inputs to each module.

2. Look-up table and a generator of the coincidence signal.

3. ORed module from 4 look-up table modules.

They have worked since Nov. 1989 without any trouble.

Appendix C

Beam test of hadron response in the LG calorimeter

To obtain the hadron response in the LG calorimeter, the beam tests are performed by using the test beam of the KEK-PS. Measurements are performed at energies of 1, 2, 3, and 4 GeV, with the true and pion beams. Fig. C.1 shows the experimental set-up in the T2 beam line at KEK-PS. Upstream gas Čherenkov counters are used at various pion discrimination. The counters T1, T2, T3, and T4 are trigger scintillation counters. The information from the drift chambers BDC1 and BDC2 is used to determine the beam position, but it is not really needed in this analysis. The X-ray drift chambers TRD1, TRD2, TRD3, and TRD4 are for X-ray detection and they are also not needed. The veto counter or counters are settled in front of the LG counter and used to reject the beam halo. Seventeen LG counter are put in as a 3 x 3 array. The beam are incident on the center of the LG modules of the 3 x 3 array. Energy calibrations for the LG counter are performed by the electron beam.

Figure C.1: Experimental setup for the beam test of the LG calorimeter

Appendix C

Beam test of hadron response in the LG calorimeter

To obtain the hadron response to the LG calorimeter, the beam tests are performed by using the test beam of the KEK-PS. Measurements are performed at energies of 1, 2, 3, and 4 GeV, with electron and pion beams. Fig. C.1 shows the experimental set-up in the T2 beam line at KEK-PS. Upstream gas Cherenkov counters are used as electron/pion discrimination. The counters T1, T2, T3, and T4 are trigger scintillation counters. The information from the drift chmabers BDC1 and BDC2 is used to determine the beam position, but it is explicitly needed in this analysis. The Xeon drift chambers TRD1, TRD2, TRD3, and TRD4 are for X-ray detection and they are also not needed. Two veto scintillation counters are settled in front of the LG counter and used to reject the beam halo. Downstream LG counters are put in as a 3×3 array. Test beams are incident on the center of the LG modules of the 3×3 array. Energy calibrations for the LG counter are performed by the electron beam.
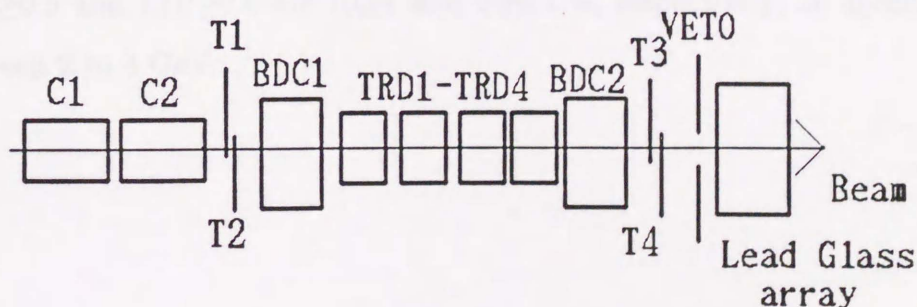
Figure C.1: Experimental setup for the beam test of the LG calorimeter
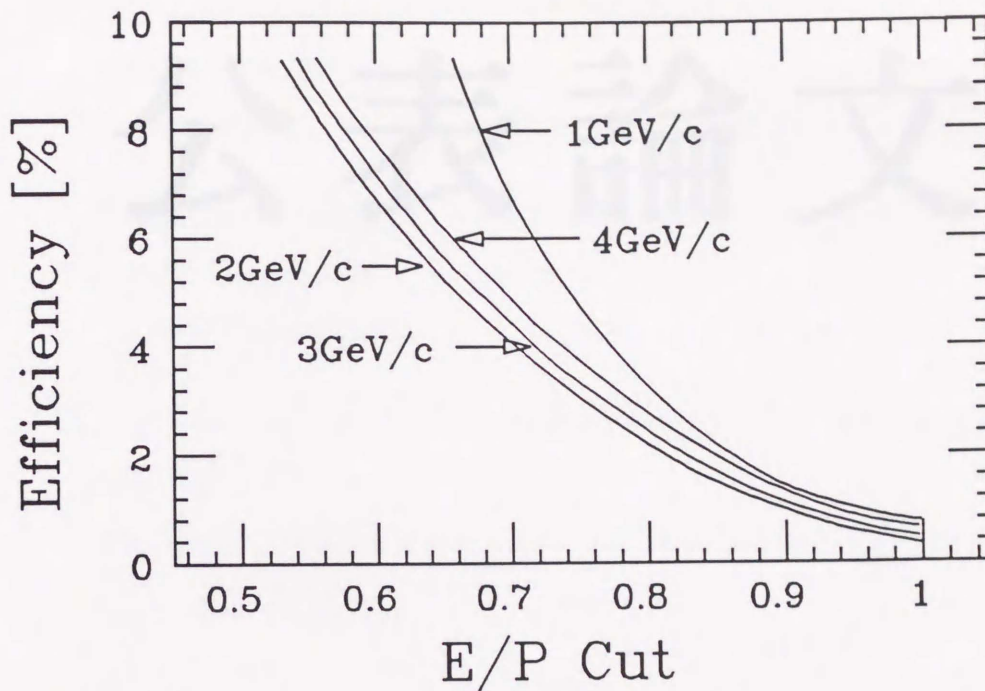
Figure C.2: The effciency of charged pion as a function of E/P cut.

Each data point for pion beam contains more than 10^6 events. The energy resolution is found to be 4% at 2 GeV. The deposit energy distributions are normalized by the energy of incident charged pions at each injection energy. They correspond to the E/P distributions expected to be realized in the VENUS. Figure. C.2 shows E/P cut efficiencies for pions obtained from beam tests. Since there are two peaks in the deposit energy distribution by charged pion, which exist at 200 and 600 MeV, the behavior of the effciency for 1GeV pion is different from that at other energies. For a small contribution to a region E> 1GeV in 1GeV-pion runs, the corresponding data are excepted from the analysis of section 5.1.1. The detection efficiency of pions for E/P≥0.5 and E/P≥0.8 are 10±1 and 2±0.5 %, respectively, at injection energies between 2 to 4 GeV.